ITER-Relevant First Mirrors Unit With Integrated Mirror Cleaning System Utilizing Capacitive Coupled RF Discharge

Dmitry Samsonov, Andrey Kamshilin, Gennadii Marinin, Denis Terentev, Ivan Kirienko, Eugene Mukhin, Victor Modestov, Georgiy Marchiy, Ivan Tereschenko, Meder Minbaev, Pavel Shigin, Lucas Moser, and Michael Walsh

***Abstract*— Basic principles are discussed for a first mirrors unit (FMU) design for International Thermonuclear Experimental Reactor (ITER) optical diagnostics, equipped with an RF capacitive coupled discharge cleaning subsystem. A nontunable RF prematcher device is shown to be desirable in the proximity to the discharge load to avoid excessive heating of an in-vessel RF feeder part. A possibility of satisfactory RF prematching with a simple nontunable L-shaped circuit is demonstrated for the experimentally measured RF discharge impedance variation. The structure of an FMU RF power distribution circuit is suggested, consisting of an RF prematcher, an RF power meter, and, when required, an RF decoupler of a DC-grounded water-cooled mirror. Planar implementation of an RF prematching device is recognized as the most feasible and universal, as a result of analysis of various base element types. Three options of RF-decoupled mirror cooling manifolds are discussed, revealing an optimal selection of their electric and dimensional parameters. A structural implementation of a planar RF prematcher ceramic parts fastening is suggested, taking into account their integrity under inertial, neutron, and thermal loads expected during ITER operation. Successful pilot tests of the RF prematcher performance and structural integrity demonstrate the promise of the described design approach.**

***Index Terms*— Ceramic parts fastening, electro-thermal device modeling, first mirrors unit (FMU), full-wave simulation, impedance matching, International Thermonuclear Experimental Reactor (ITER) optical diagnostics, passive devices and circuits, planar circuits, plasmas, RF mirror cleaning, RF power distribution.**

Manuscript received 3 January 2024; revised 17 May 2024; accepted 21 May 2024. Date of publication 11 June 2024; date of current version 13 September 2024. This work was supported in part by the ITER Organization for providing Conceptual Design of the First Mirrors Unit, Equipped with the RF Mirror Cleaning System, under Contract 4200003194 and Contract 4300001626; and in part by the Ministry of Science and Higher Education of the Russian Federation for providing the Finite-Element Structural and Thermal-Electric Simulations, under Contract 075-15-2022-311 and Contract 0034-2019-0001. The Associate Editor coordinating the review process was Dr. Tuan Guo. *(Corresponding author: Dmitry Samsonov.)*

Dmitry Samsonov, Eugene Mukhin, Georgiy Marchiy, Ivan Tereschenko, and Meder Minbaev are with the Laser-Aided Diagnostics of Plasma and Plasma-Surface Interactions Laboratory, Ioffe Institute, 194021 Saint Petersburg, Russia (e-mail: d.samsonov@mail.ioffe.ru; e.mukhin@mail.ioffe.ru; georgiy.marchiy@mail.ioffe.ru; i.tereschenko@mail.ioffe.ru; meder@mail.ioffe.ru).

Andrey Kamshilin is with HFP, 394030 Voronezh, Russia (e-mail: kaa@hfpower.ru).

Gennadii Marinin and Denis Terentev are with Russian Technologies, 195279 Saint Petersburg, Russia (e-mail: rtechster@gmail.com; den2006@list.ru).

Ivan Kirienko and Victor Modestov are with the Mechanics of Materials Laboratory, Peter the Great University, 195251 Saint Petersburg, Russia (e-mail: kirienko_id@spbstu.ru; vmodestov@spbstu.ru).

Pavel Shigin, Lucas Moser, and Michael Walsh are with the Port Plugs and Diagnostics Division, ITER Organization, 13067 Saint Paul Lez Durance, France (e-mail: Pavel.Shigin@iter.org; Lucas.Moser@iter.org; Michael.Walsh@iter.org).

Digital Object Identifier 10.1109/TIM.2024.3412226

I. Introduction

PROTECTION and maintenance of optical components faced in the present-day fusion devices are expected to be a far more serious problem for the next-step burning plasma devices. All in-vessel optical components of International Thermonuclear Experimental Reactor (ITER) diagnostics are being designed and developed to be subjected to severe environmental conditions while they typically need to meet high requirements for optical stability. Along with stability of the spatial position and shape of the reflecting surface, this means retaining specular reflectance in a spectral range specific to each optical diagnostic.

Contamination with plasma-induced erosion products is one of the recognized reasons for the decrease in reflectivity of the "first" mirrors (FMs), located in the line-of-sight of the fusion plasma [1], [2]. Deposits result in a significant reduction and spectral alterations of optical elements. Even fairly thin and transparent deposits can change dramatically the mirror reflectance spectra due to the interference phenomena [2], [3]. Distortion of data obtained with various optical diagnostics may impact the ITER safe operation. Therefore, the development of in situ cleaning and deposition-mitigating techniques is a key factor in the construction and operation of optical diagnostics in ITER. A number of FMs must be actively cleaned in order to retain reflectivity during the machine lifecycle.

Currently, treatment of contaminated mirror surfaces with ions extracted from a local DC/pulsed DC [4] or RF [5] discharge is the primary candidate technique for mirror cleaning in ITER. The main focus has been on RF discharge plasma, which is intended to eliminate both conductive and dielectric contaminants with minimal damage to the mirror surface. To implement RF cleaning, the FMs must be equipped with an appropriate local capacitive RF discharge subsystem, assuming that the discharge is excited between the mirror, acting as an RF-driven electrode, and the surrounding structures operating as a grounded electrode.

The first mirrors unit (FMU) is typically located behind the diagnostic first wall (DFW) [6], [7]. In major of optical

diagnostics, it is presented by paired mirrors in a dog-leg configuration, aimed to suppress streaming neutrons and radiation flux along the optical path. This "periscopic" configuration considers two neighboring mirrors, that in practice requires cleaning both of them due to contamination particles transport features and/or redeposition during the cleaning process.

The severe ITER conditions impose certain constraints on an FMU design. Mirrors, as well as surrounding structures, may require active water-cooling. Limited space typically reserved for the FMUs requires minimizing the dimensions of the equipment accompanying the FMs.

The effectiveness of the RF mirror cleaning can be characterized by an average cleaning rate and spatial homogeneity. They depend on the bombarding ions' energy and current density spatial distributions over the mirror surface. The latter, in turn, is determined by the RF power supplied to the discharge plasma, the discharge excitation frequency, gas composition and pressure, the relative position of RF electrodes, the geometry of surrounding structures, and external B-field direction/magnitude [8], [9]. For each contamination species, these parameters should be selected, considering maximum cleaning efficiency, while maintaining the required mirror optical properties along its service life. The mirror cleaning technological scenarios are being developed in accordance with ITER policies [10], [11].

The amount of RF power, required to clean a mirror, is mainly determined by its dimensions and the external electrical circuit that feeds the discharge. The operating frequency and gas species are selected, taking into account the so-called cleaning selectivity, i.e., the ratio of sputtering rates of contaminating deposit and mirror material [9]. The gas pressure primarily affects cleaning spatial homogeneity and transport of redeposited material. A combination of discharge geometric and operating point parameters, as well as an external feeding circuit, determines its properties as an electrical load.

Guidelines for choosing an RF mirror cleaning subsystem parameters values are currently being elaborated in the course of a broad front of research and development initiated by the ITER Central Team in collaboration with Domestic Agencies, and address both the physical and technical aspects of the problem. Topics covered include the resistance of candidate mirror materials to damage by impinging ions [12], the effectiveness of cleaning various contaminants in different discharge operating conditions [13], [14], [15], the dependence of plasma parameters on electrode geometry [16], the sputtered neutrals transport [17], the spectroscopic end-of-cleaning indicator [16], the influence of the supplying electrical circuit [18] and of external magnetic field [19] on the cleaning RF discharge, the effect of grounded surfaces sputtering [20], and the potential plasma-chemical effect of D_2 on contaminants removal [21]. The findings of extensive laboratory research to date allow for limiting the considered RF power range, in most cases, from 200 to 2000 W, and the frequency range from 10 to 100 MHz. The most likely gas choice is He, which is less damaging to the mirror surface [15], [13], although Ne, Ar, and D_2 are also being explored as having widespread atomic masses among the accessible gases.

Detailed development of the mirror cleaning scenarios requires taking into account the feasibility of the RF discharge power supply system in an ITER environment. The general requirements are described in [22] and [23], as well as the problems that arise during the transition from research on RF mirror cleaning to implementation in a real FMU, and the first experiments reproducing the operation of parts of a real ITER RF mirror cleaning system.

In [24], experiments on RF mirror cleaning are presented in a realistic ITER 55.C2 Edge Thomson Scattering periscope configuration with $\sim 250 \times 200$ mm^2 mirrors at a distance of 20–30 cm. Comparable average energies of ions bombarding the electrode were achieved for both DC-decoupled and DC-coupled mirror-electrode, with the comparable values of RF power delivered to the discharge. The ion flux in the latter case was 10 times higher. The ion energy and flux onto the grounded walls adjacent to the mirror was comparable to that onto the mirror. The ion flux reduced by tens of times with distance from the mirror, while the ion energy decreased by $\sim$4 times, ending up near the wall material sputtering threshold. It was found that the discharge gets unstable as supplied RF power increases above 400 W. These circumstances highlight the importance of properly selecting the design and materials of the surrounding ground surfaces. The cleaning rate was different several times across the mirror surface, taking values of order 1–10 nm/h for various metal and oxide contaminants at an ion energy of $<$150 eV for a 40 MHz He discharge.

The purpose of this article is to present the basics and some key radio engineering and mechanical engineering details of a possible approach to an FMU design, equipped with an RF cleaning system.

The ITER IO selected the ITER 55.G6 IR Thermography diagnostics as an exemplary system for developing conceptual FMU design since it shares some key design constraints with a number of other systems: two water-cooled mirrors that are relatively close and of average dimensions, the FMU is not located in the DFW or deep within the diagnostic shielding module (DSM), and no mirror cleaning functions were implemented prior to the start of work. This system is aimed on monitoring the surface temperature and the power loads on the ITER divertor targets and the related baffles. The mirror optical stability is being solved within the separate study, and is not discussed here.

This article is structured as follows. Section II provides the problem formulation and general description of the developed FMU concept. Section III discusses the principles for the development of an FMU RF power distribution circuit, including the characterization of an RF discharge plasma as an electrical load, and RF power distribution circuit implementation options with a focus on planar design. Section IV is devoted to the mechanical design of the planar RF prematching device, including the approach to fastening the ceramic plates of the RF planar prematcher, and ensuring their integrity under ITER-relevant inertial, thermal, and neutron loads. Section V describes the pilot experiments to address the operability and structural integrity of the planar RF prematcher.

TABLE I
INPUTS FOR 55.G6 FMU DEVELOPMENT

Mirror #	M1	M2
Surface area (cm^2)	52	127
Angle between the surface normal and the B-field (deg)	60	45
Mirror surface shape	Planar	
Distance between mirrors (mm)	196 (shortest) 250 (centers)	

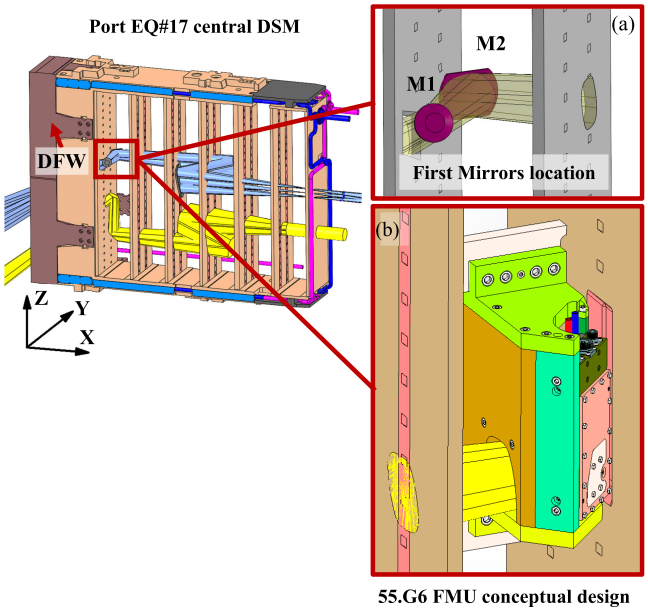

Fig. 1. (a) Location of the 55.G6 FMs. (b) 55.G6 FMU arrangement, developed for installation into the EQ#17 DSM.

II. DESIGN AND INTEGRATION OF THE 55.G6 PERISCOPIC FMU

The 55.G6 IR Thermography front-end optics is located in the ITER Equatorial port EQ#17 and is based on a double-mirror periscope. Both mirrors marked M1 and M2 in Fig. 1(a) must be water-cooled, since they will be subjected to intense neutron and gamma irradiation, resulting in a high volumetric heat release. The FMU location in the DSM of the port EQ#17 is shown in Fig. 1(a), while the main quantitative input parameters are summarized in Table I.

Both mirrors must be supplied with RF power to enable their independent cleaning. The need to connect metallic cooling tubes to the mirrors is imposed using an RF power supply scheme, which is compatible with a DC short-circuited mirror-electrode [10]. To reach effective cleaning, such a scheme requires a power of 1–2 W*cm^{-1} to be supplied to the mirror-electrode [18]. The highest cleaning selectivity for He is reached at the frequency of 80 MHz [9].

Closely spaced and cross-influencing FMU subsystems, such as the mirror fastening unit and the RF mirror cleaning system, suggest their joint development. To ensure controlled integration as well as smooth optical and electrical initial adjustments, it is also desirable to isolate the FMU in a

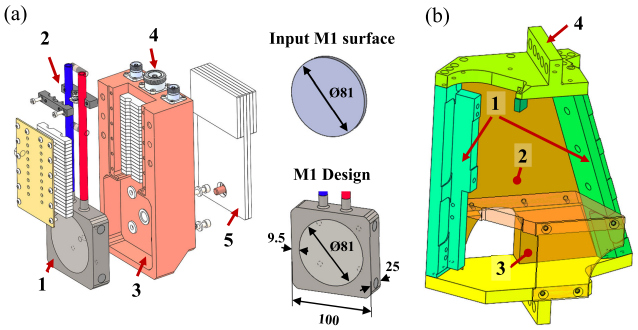

Fig. 2. Detailed view of the 55.G6 FMU conceptual design. (a) M1 mirror assembly. (b) FMU housing.

separate assembly. Fig. 1(b) shows the arrangement of the 55.G6 FMU in the EQ#17 DSM, developed following the mentioned principles.

The DSM design proposed by the ITER Central Team is used for port EQ#17. It is made as frames with vertical bulkheads [see Fig. 1(a)], assuming, that the diagnostic equipment is mounted between them, and the remaining volume is filled with neutron shielding blocks. The installation and removal of the designed FMU are intended to be compatible with remote handling (RH) procedures [25]. To compensate for the possible influence of insufficiently rigid bulkheads on the stability of the mirrors angular position, the M1 and M2 mirror assemblies, located in the immediate vicinity of the DFW of the DSM, are structurally united by a single supporting structure. The developed FMU has overall dimensions of 535 × 475 × 170 mm and a weight of ∼90 kg. Two mirror assemblies of a similar design [see Fig. 2(a)] are mounted on a rigid self-supporting housing [see Fig. 2(b)].

Each of them is equipped with an RF plasma cleaning system and consists of a mirror body [see Fig. 2(a-1)], water cooling tubes combined with the RF-decoupler [see Fig. 2(a-2)], case combined with electric shields [see Fig. 2(a-3)], RF electrical connectors [see Fig. 2(a-4)], and the individual planar RF power distribution circuit [26], consisting of the prematching system and the RF power sensor [see Fig. 2(a-5)]. The water tubes are welded to the mirror body and DC-grounded, following the ITER Electrical Design Handbook requirements [27, Sec. 8]. The RF-decoupler is designed as a shorted quarter-wave transmission line stub, filled with dielectric to reduce physical length, and to prevent parasitic breakdown. The RF-decoupler has no bends between the mirror and the grounding point which improves its feasibility.

After the grounding point, the water tubes no longer need to be shielded and could therefore be bent. This allows for their optimum routing upon the interfacing point with the DSM cooling circuit, providing also enough space to comply with orbital welding and other RH requirements.

Along the mirror edges, the so-called sacrificial areas with a width of ∼10 mm are introduced, where the cleaning will be unavoidably highly inhomogeneous due to the edge effect. The mirror body is electrically isolated from the grounded case through dielectric inserts at the attachment points. The vacuum gap of 1 mm thickness is arranged between the mirror body

and the case, which is small enough to prevent ignition in this gap of a stable RF discharge even in an easily ionizable gas.

The mirror assemblies are nested on the seats [see Fig. 2(b-1)] on the housing [see Fig. 2(b)]. The space reservation [see Fig. 2(b-2)] for a shutter driver is allocated inside the dust-protected volume. The housing elements are arranged to form a grounded shell enclosure [see Fig. 2(b-3)] around the light path, preventing dust penetration to the mirrors. This shell enclosure is also important for the volume shape control, where the RF discharge plasma exists, in order to tailor the E-field distribution. This helps suppressing local parasitic nonself-sustained RF discharges, as well as shaping RF discharge plasma to improve cleaning uniformity and suppress/redirect/sink unwanted walls sputtering and redeposition by local surface features: patches of biased electric potential, surface texturing, low-sputtered material, etc. [20]

The housing is attached to the DSM bulkheads via interface panels (4), one of which also accommodates a RH electrical connector. In order to dissipate neutronic heat flow, both the supporting structure and mirror assembly housings may require active water cooling, in addition to the mirrors.

Some of the features of the presented FMU can be compared with those of other systems being developed in parallel. The FMU of ITER 55.E1 Core-plasma CXRS system [28] comprises a "stacked" structure consisting of a housing mounted on the DSM and recessed in the DFW, a $\sim 85 \times 170$ mm^2 FM, a cooling block, and an adapter flange for mirror alignment. Indirect active water cooling of the mirror is provided by structural contacts with the cooling block via 10 mm thick ceramic plates, which also operate as electric insulation, enabling supplying electric potential to the mirror to drive the cleaning discharge. The mirror rear surface is insulated with a gap of <2 mm to grounded surfaces. An interesting design feature is the ability to replace the mirror with no need to readjust it. The mirror is preassembled in an appropriate environment with a cooling block, and when replaced, this assembly is attached to a flange that was once adjusted and secured to the FMU housing. The DSM is employed as a common "optical bench" for the three front end mirrors. These features are mentioned to demand very high manufacturing and assembly precision for the entire FMU, as well as an even higher precision for the mirror assembly with the cooling block. The extensive design coordination with the port integrator is anticipated as well. During the system lifespan, 100–500 mirror cleaning cycles with a 60 MHz RF discharge are projected. To this end, the design features a rigid in-vessel coaxial RF feeder with no additional RF power distribution devices. The electrical circuit analysis, which confirmed the efficiency of this approach, is yet not presented, however. Some design components, like the electrical interface between the mirror and the RF feeder, appear to have been initially designed for DC cleaning, because, as described in [29], the final choice between DC and RF cleaning was not taken during earlier development phase, which also claims a more detailed analysis of RF performance [30]. The indirect mirror cooling approach, which appears to have also originated from DC cleaning, appears to be simpler from an "electrical" viewpoint, and more robust than the direct active cooling considered here. However, its applicability to an arbitrary system may be limited by the ability of the thermal interface to sink heat at specific ratios of incident radiation to mirror size.

The FMU of the ITER 55.G1 Wide Angle Viewing System [31] is equipped with two dog-leg mirrors, secured on a common flange ensuring their relative alignment, and a pneumatic shutter. A distinctive feature of this FMU is a conical element (called a pyramid) limiting the field-of-view to avoid parasitic light. All elements are enclosed inside the housing, which consists of three parts. Despite all elements of the FMU including mirrors and the housing being actively cooled (via Ø4 mm water channels), the average mirror temperature of 165 °C is expected during operation. Mirror assemblies are cooled indirectly with the use of a 2.5 mm thick Al_2O_3 ceramic insulating layer between the stainless steel 316L(N)-IG optical mirror and the CuCrZr-IG substrate with water channels, which are screwed through multiple RF-insulating ceramic T-spacers. As with the proposed design, the structural integrity of these T-spacers, together with their influence on mirror surface distortion, demands further investigation. It is noted [32] that FMU mirrors may require some position corrections during the diagnostic commissioning to partially compensate for various residual adjustment errors, resulting from intrinsic modeling uncertainties (e.g., thermal expansion coefficients values and potential discrepancies with respect to the built).

Given optical inputs, structural, and other constraints, the FMU design starts with determining the electrical parameters and the elemental base of the RF power distribution circuit, since they have a decisive influence on the design along with ensuring the stability of the position of the reflecting surfaces. After that, housing is constructed around the electrical elements, taking into account the requirements for the shape of the shell enclosure, the available space reservation, and RH requirements.

III. RF Power Distribution Inside the FMU

The design of any electrical system starts with defining the load parameters, which is complex impedance Z_L in the case of an RF load. Unlike broadcasting systems, where RF load is typically an antenna with almost constant impedance, the RF discharge impedance is subject to some variation, depending on the operating point: driving frequency f and power W, working gas composition and pressure p. In technological vacuum facilities utilizing RF discharge, the problem of changing load impedance during the process is commonly solved with tunable RF matching devices, located outside the vacuum chamber. Unlike laboratory systems that operate in normal environments, the in-vessel components of an RF power distribution system in ITER will be subjected to intense thermal, inertial, and irradiation loads. This circumstance severely restricts the range of applicable design solutions and materials.

A. Measurement of the RF Discharge Load Impedance

The initial guess of Z_L for further calculations of the RF power distribution circuit was revealed from a series of

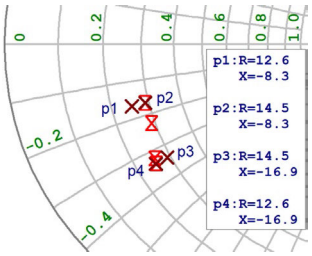

Fig. 3. Measured RF load impedance values $Z_L = R + jX\Omega$.

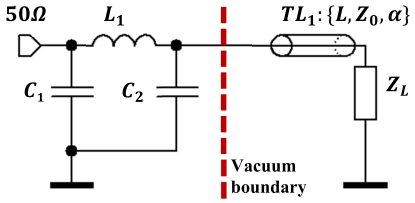

Fig. 4. "Classic" RF discharge power supply scheme with an ex-vessel RF matching box.

capacitive RF discharge load impedance measurements. The measurements on the 55.G6 FMU mock-up mirror-electrode M1 were taken using an ex-vessel RF matchbox. The mirror electrode measured 100 × 100 mm and had a vacuum gap of ∼1 mm. There was no external magnetic field applied. The load impedance Z_L was measured for He in the pressure range of $p = 1.5 - 10$ Pa and Ar at $p = 0.7 - 7$ Pa. The driving RF power W ranged from 50 to 300 W, and the frequency was $f = 81.36$ MHz. The measurements were carried out using the two-step method discussed in Appendix I. The load impedance Z_L of interest is hereinafter defined as the capacitance of the rear side of the electrode, connected in parallel with the RF discharge plasma impedance. The measured Z_L values are presented on the normalized Smith chart in Fig. 3. To facilitate further analysis, the measured points cloud is restricted to the continuous region, bounded by points $P_1, \ldots, P_4$.

Despite the measurements being taken over a wide range of discharge operating parameters, the measured Z_L values turned out to be concentrated in a fairly narrow region. This can be explained by the fact that the "constant part" of Z_L, i.e., mainly the electrode backside capacitance, contributes more than the "variable part," which is the RF discharge plasma impedance.

B. Analysis of the RF Power Distribution Circuit Structure

It is worthwhile reviewing the applicability to the ITER environment of a "classic" RF discharge power supply scheme with a tunable LC matching device, which is commonly employed in technological facilities. In ITER, the tunable matcher can only be located ex-vessel (see Fig. 4).

It is connected to the load impedance Z_L by a section of the Ø6 mm mineral insulated (MI) coaxial cable which is assumed at ITER as an in-vessel feeder for RF power delivery to mirror cleaning systems. The cable segment TL_1 has a length L, relative dielectric permittivity $\varepsilon_r \approx 2.5$, characteristic impedance $Z_0 \approx 50\Omega$, and attenuation α in the range of $0.15 - 0.3$ dB/m, depending on temperature [33].

TABLE II
OPTIMAL RF DISCHARGE POWER SUPPLY CIRCUIT PARAMETERS USING AN EX-VESSEL RF MATCHING BOX

L (m)	Z_0 (Ω)	C_1 (pF)	L_1 (nH)	C_2 (pF)	P_L (%)
5	50	191	47	165	54
	18	106	58	134	64
8	50	196	38	176	41
	17	111	43	173	51

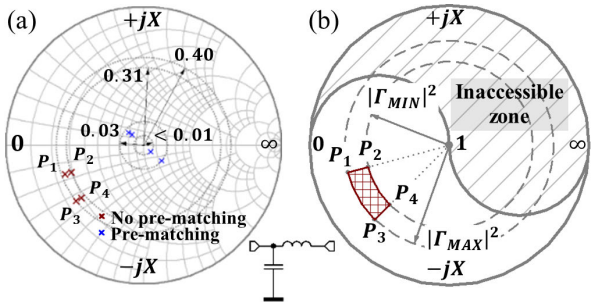

Fig. 5. Effect of RF impedance prematching on the reflected power. (a) RF power reflection from the load without matching (red) and with prematching (blue) using and LC circuit with $L \approx 71\ nH$; $C \approx 64\ pF$. (b) L-shaped network suitable for prematching the RF discharge load impedance.

The upper loss estimate is taken in the calculations below, since the cable will heat up during operation.

The length L will be at least 5 m for the ITER equatorial ports, and ∼8 m for the divertor ports. Without loss of generality, the example $Z_{L0} = 13.6 - j12.3\ \Omega$ is taken, which corresponds to the center of the region $P_1, \ldots, P_4$ in Fig. 3.

Table II displays the numerically optimized values of C_1, L_1, and C_2 for the best load matching, i.e., the lowest reflected power and the highest power P_L deposited in the RF load. The cable and the load are the only lossy elements in this circuit, hence the loss in the cable is $P_F = 100\% - P_L$. The calculation was performed for two Z_0 values: conventional 50 Ω and the one providing the highest P_L. In the latter case, Z_0 remained free throughout the optimization.

The calculations above indicate that the optimal Z_0 value is close to $|Z_L|$. In this case, the maximum P_L would be 64% or 51%, however, this would require the use of a nonstandard cable. In other cases, P_L will be 54% or 41%, which is explained by the highly lossy MI cable section becoming part of the oscillatory RF circuit. Instead of this not-very-efficient discharge power supply scheme, an RF "prematching" circuit could be installed in the immediate vicinity of the load to correct its parameters in such a way as to increase P_L and reduce P_F.

1) Idea of a Nontunable RF Load Impedance Prematching: The region of Z_L variation [see Fig. 5(a)] is bounded by circles of equal RF power reflection $0.31 \le |\Gamma|^2 \le 0.40$.

Without impedance matching, this requires roughly triple the input power, and nearly doubling it in the case of a MI cable with high loss used as the in-vessel feeder part. This is undesirable because the total input power is limited by the capabilities of the vacuum feedthroughs and MI cables, considered for use in ITER.

An RF prematching device located in close proximity to the load would allow for minimizing the RF circuit section between the impedance matcher output and the load, which is where the increased reactive power and, hence, loss are concentrated. Given the limited range of materials and technologies permitted for use inside the ITER vacuum vessel, the design of such a device should be extremely simple and, if possible, require no adjustments after installation.

The simplest RF matching circuit is an L-shaped circuit with two reactive elements. At a fixed frequency, such a circuit transforms any single impedance point into any other target value [34]. Nonadjustable circuits cannot reduce an impedance region to a single point. However, for a limited Z_L variation region, the spread around the target impedance can be small enough to effectively reduce the RF power reflection and heat load on the RF feeder in-vessel part.

There are eight possible L-shaped LC circuit structures [34], each capable of matching a semi-infinite region. Certain of them should be picked so that the region of Z_L variation is entirely within this permitted region. Fig. 5(b) depicts an L-shaped circuit, that meets this condition, providing the region of matched Z_L standing far enough from the "inaccessible zone" boundaries.

The parameters of the matching circuit were chosen by numerical optimization. This optimization goal was to find L and C, which provide the transformed impedance values region fit inside the circle of the lowest $|\Gamma|^2$. At $L \approx$ 71 nH and $C \approx$ 64 pF, the transformed impedances [see Fig. 5(a)] fit within circles $0.005 < |\Gamma|^2 < 0.03$. The feasibility of the obtained values should also be concerned. Too low L and C values will cause challenges in manufacturing and adjusting, as well as a large influence of parasitic reactance, affecting operational stability. Implementing too big values may appear challenging due to parasitic self-resonances, as well as structural integrity and integration considerations.

In the presented RF cleaning system architecture, the mirror-electrode must be water-cooled. The delivery of cooling water to the mirror-electrode via metallic tubes introduces some additional impedance, plugged in parallel to it. A poor choice of this impedance value will result in inefficient RF power deposition into the discharge, as well as RF electrode voltage drop, hindering discharge ignition. To achieve reliable RF decoupling without interfering with the rest of the circuit operation, the decoupler input impedance $|Z_F|$ must be much higher than the load impedance $|Z_L|$.

In order to monitor in situ the discharge state, it is highly desirable to install an RF power sensor close to the load. Directional coupler is currently considered the most ITER-compatible sensor type. Given the significant attenuation of the reflected wave in MI cable over long distance between signal detection and measurement points, a signal level of several Watts is desirable for stable measurement. This suggests a coupling coefficient of -25 dB would be sufficient. To measure not only P_L, but also Z_L, a directional coupler with a tailored design should be positioned between an RF prematcher and a load.

Fig. 6 demonstrates a block diagram of the FMU RF power distribution circuit, summarizing the findings of the study.

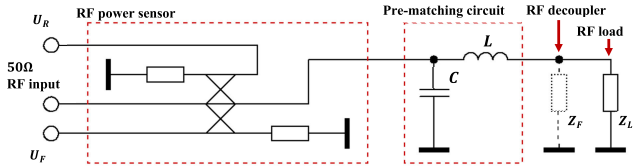

Fig. 6. Block diagram of the RF power distribution circuit inside the FMU mirror assembly.

Together with the RF power distribution block diagram definition, an ITER-compatible element base should be determined for its implementation. This defines the feasible range of element values, their dimensions, power handling capability, etc.

C. Element Base for the RF Power Distribution Circuit

The choice of an RF circuit's basic elements is determined by its electrical operating modes, available materials, and the proposed design solutions. Unfortunately, the applicability limit for both lumped and distributed elements appears within the considered frequency range of 10–100 MHz [35]. Due to dimensional features, lumped elements may have self-resonances and parasitic interactions at 30 MHz, leading to the risk of miscalculation, tuning instabilities, and subsequent uncertainty in the resulting circuit properties [36], [37]. In turn, distributed elements at 60 MHz typically have dimensions, comparable to those of surrounding structures in the ITER port, which complicates their arrangement inside the available space reservation. Deviations from the expected parameters may also arise at short electrical lengths, due to a breach of the assumptions under which the distributed-element models are valid.

The subject of the following analysis is to reveal the limits for Z_L matching, achievable using various basic elements, as well as reflection and insertion loss provided by an RF power distribution scheme that utilizes them. The feasibility of an RF prematcher employing various basic element types was investigated, including coaxial stubs, lumped LC elements, stacked coaxial junctions [38], and planar distributed elements [39], [40].

1) RF Prematcher Based on MI Cable Stubs: As a starting point, estimates for two RF prematching circuits are provided below, based on short-circuited MI cable stubs. The trivial case of a matching circuit according to Fig. 5(b) is the reactance Z_{TL}, connected in parallel to Z_L [Fig. 7(a)]. In this case, a single reactive element is utilized rather than two. A detailed discussion in Appendix II reveals that despite a considerable power performance, it only allows matching a limited range of Z_L.

In turn, a prematcher with two stubs [Fig. 7(b)] allows for matching Z_L over a considerably wider range, but at a cost of ~25% power loss and difficulties with precise initial adjustment. Therefore, an RF prematcher based on MI cables is only applicable in cases where either Z_L is assured to fall into the permitted zone, or the power budget allows dissipating ~25% without overheating the feeder components. The finite-element method (FEM) estimates 320 °C for a

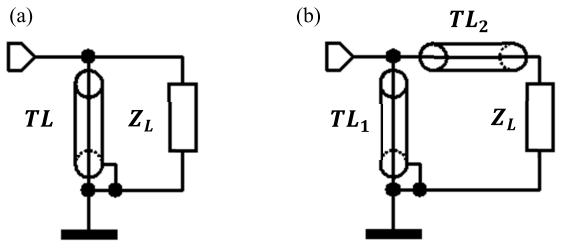

Fig. 7. Schematic of an RF prematcher utilizing short-circuited MI cable stubs. (a) Single stub. (b) Two stubs.

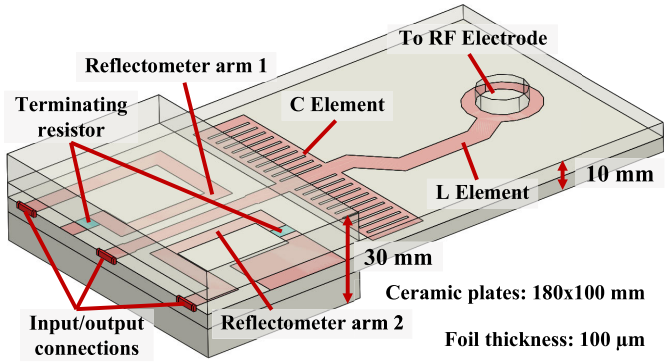

Fig. 8. Planar implementation of an RF power distribution circuit, consisting of an L-shaped LC prematcher and a reflectometer.

total dissipation of ~35 W/m in the MI cable. The maximum allowable mirror surface area therefore depends on actual stub lengths and is estimated to be 200 cm^2.

2) RF Prematcher Based on a Planar LC Circuit: Lumped elements were rejected due to difficulties in preventing RF breakdown and arrangement. The electrical and dimensional efficiency of the prematcher utilizing stacked coaxial junctions [38] was no worse than that of planar elements. However, planar elements were chosen for this specific application, since they provide a flat layout, which turned out to be more feasible in the available dimensions. This choice was also made easier because planar RF reflectometers are more compact and advanced in manufacturing and adjustment.

Fig. 8 shows an example of a planar board layout, which implements the circuit illustrated in Fig. 6. It contains the L and C elements, located on the common dielectric plate with the bi-directional RF reflectometer. Alternatively, planar elements can be stacked to save space.

To ensure acceptable current density, the thickness of the planar conductors should be at least five RF field skin depths. Considering margins for the surface roughness and current density inhomogeneities, this results in a values range of 50–100 μm. The dielectric thickness of 10 mm in the prematcher zone is chosen mainly to achieve the required C value, with little effect on the L value. In the reflectometer zone, it is selected to ensure a given characteristic impedance of the corresponding transmission line segments. When the reflectometer is behind the prematcher, it requires a characteristic impedance of 50 Ω to operate correctly, resulting in a dielectric thickness of ~30 mm. All planar conductive topology elements are arranged in the middle between the ceramic plates. Section IV discusses the structural implementation of a planar

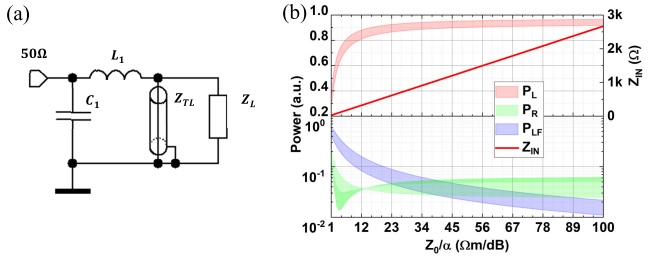

Fig. 9. (a) Circuit schematic showing a shorted $\lambda/4$ RF decoupler. (b) Circuit power balance.

RF power distribution board, including the choice of dielectric material and metallization technology.

3) Shorted λ/4 RF Decoupler: The most promising and studied [10] way of RF decoupling the water-cooled mirror-electrode utilizes structural combining the water supply tubes with the so-called "metallic insulator"—a short-circuited RF transmission line stub with a length of 4 of an operational wavelength λ. The tubes are connected to the cooled mirror base on one end and grounded on the opposite end. After this grounding point, the tubes routing has no effect on the qualities of an RF decoupler.

The input impedance of a lossy shorted stub is defined as

$$Z_{TL} = Z_0 \tanh(\alpha l + j\beta l) \quad (1)$$

where Z_0 is the stub characteristic impedance, α stub line attenuation, $\beta = 2\pi/\lambda$——line propagation constant, and l—stub segment physical length. When tuned ideally, a lossless ($\alpha = 0$) stub does not impact current and voltage distributions in the rest of the circuit, as $|Z_{TL}| \to \infty$. Nonideal tuning ($l \neq \lambda/4$) makes both l and Z_0 impacting currents and voltages in the rest of the circuit. On the one hand, this can be utilized as a degree of freedom in circuit optimization, enabling even simplification of an RF prematcher by removing one of the LC elements. On the other hand, this complicates circuit analysis and tuning. In the design described here, the choice is left to an ideally tuned RF decoupler, whereas the case of a reduced length will be analyzed in further development. In a lossy line ($\alpha \neq 0$), when $l = \lambda/4$, expression (1) simplifies to $Z_{TL} = Z_0 \coth(\alpha l) \approx Z_0/\alpha l$. Thus, as α increases, Z_{TL} becomes real and decreases, requiring careful consideration during detailed development.

A circuit schematic along with the circuit power balance in dependence on Z_0/α ratio is shown in Fig. 9.

Dielectric permittivity $\varepsilon_r = 8.3$ is assumed for the ceramic filling, which corresponds to $l = l_0/(\varepsilon_r)^{1/2} \approx 326$ mm, where l_0 is length with vacuum filling. For the assumed Z_L, the P_L reaches 90% when $Z_0/\alpha \approx 49$ Ω m/dB, which corresponds to $Z_{TL} \approx 1.3$ kΩ.

The coaxial line appears to be the most promising transmission line type for building an RF decoupler. Being shielded by design, it provides no radiative RF power loss and no interaction with surrounding structures or the RF discharge plasma. For example, to avoid such undesirable interaction, an unshielded twin line requires a distance of at least 5–7 distances between its conductors and the surrounding structure [41, Section 11.5], [42], [43], which forces dimensions

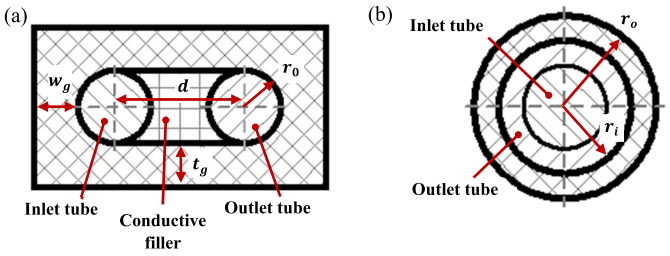

Fig. 10. Cross section of the RF decoupler with (a) separate inlet and outlet tubes and (b) nested tubes.

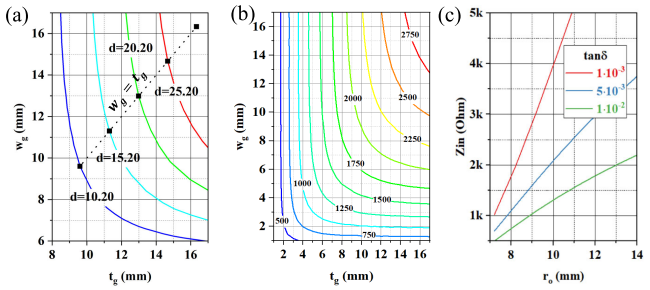

Fig. 11. Coaxial RF decoupler input impedance dependencies on geometric parameters. (a) Isolines $Z_{\text{IN}} = 2$ kΩ in dependence on d. (b) Isolines $Z_{\text{IN}} = \text{const}$ with $d = 10.2$ mm for the layout with separated cooling tubes. (c) Z_{IN} in dependence on r_o with $r_i = 5.15$ mm for the layout with nested cooling tubes.

increase. Being filled with a solid dielectric, a coaxial line appears more advantageous in mitigating parasitic discharge, while an unshielded twin line is more likely to cause parasitic plasma ignition.

For a coaxial line, Z_0 and α depend on its cross section shape, wherein α decreases with increasing Z_0. The total line attenuation α is equal to the sum of the dielectric α_D and the conductors α_C attenuation: $\alpha = \alpha_D + \alpha_C$. While $\alpha_D \sim f(\varepsilon_r)^{1/2} \tan\delta$ does not depend on the line configuration, but only on the dielectric material characteristics, $\alpha_C \sim (f\rho_C\varepsilon_r)^{1/2}F(D,d)$, where ρ_C—material resistivity, F—function, decreasing at constant line characteristic inner dimensions d with increasing outer dimensions D. The value of Z_0 at sufficiently high frequencies is expressed as $Z_0 = (\varepsilon_r)^{1/2}/cC_C$, where c is the light velocity in vacuum and C_C is the linear capacitance. Z_0 is dependent on the configuration of the line conductors and filler medium.

For a line with a complex-shaped cross section, Z_0 and α may be difficult to reveal analytically [44], but this can be solved numerically, for example, by FEM [45], [46]. The inner conductor dimensions appear to be constrained from below by the minimum outer diameter of the tubes recommended by ITER [47, Section 12.2.18, 12.2.3]. The effect of dimensions on the Z_0/α ratio is analyzed below for two design options. In respect of engineering gap, the target value $Z_{TL} = 20$ Ω is assumed.

The first design option is that the inlet and outlet cooling tubes are embedded separately in the central conductor, which drives a nearly rectangular cross section, convenient for layout design and manufacturing [see Fig. 10(a)]. The inner conductor outer surface is composed of cooling tubes and a conductive filler in between. This cross section shape is defined with four parameters: the tube outer radius r_0, the tubes center-to-center distance d, and the gap thickness along the longer and shorter sides w_g and t_g, respectively.

Another design option [see Fig. 10(b)] involves nesting the tubes one inside the other, resulting in a cross section shape similar to the well-studied circular one. To ensure undisturbed water flow, the cross-sectional areas of the inner and outer tubes should be approximately equal. For a fairly task-appropriate inner tube outer diameter of 10.2 mm and a wall thickness of 2 mm, the cross section area is 30.2 mm^2 and the minimum inner diameter of the outer tube is 12 mm.

Dependences of Z_{TL} of a shorted $\lambda/4$ line of both cross section kinds on the geometric parameters, revealed with FEM, are discussed below. Fig. 11(a) depicts a family of isolines with $Z_{\text{IN}} = 2$ kΩ as d varies between 10.2 and 30.2 mm. Smaller d demands smaller w_g and t_g. Both parameters show rather fast saturation, and neither exhibits an extremum. Therefore, d is driven mostly by "structural" rather than "electrical" considerations. Probably, d is limited from below by restrictions on the wall thickness between the water channels, whereas w_g and t_g must be set based on ceramic strength. There is no evident reason to have $w_g \neq t_g$.

For reference, Fig. 11(b) displays the Z_{IN} dependence on w_g and t_g at selected minimum value of $d = 10.2$ mm. The minimum dimensions turn out to be sensitive to the material $\tan\delta$. At low $\tan\delta \approx 10^{-3}$, conductor and dielectric losses are of the same order, while at $\tan\delta \approx 10^{-2}$, dielectric loss already has a decisive contribution to Z_{IN}. Fig. 11(c) plots Z_{IN} versus outer radius r_o for a nested-tubes line with an inner radius $r_i = 5.15$ mm. In this case, at $\tan\delta = 5\cdot10^{-3}$ the target value of $Z_{\text{IN}} = 3$ kΩ is reached at $r_o \approx 9.8$ mm.

The tube cross section, required for sufficient mirror cooling affects significantly the RF decoupler efficiency, and hence appears an important design parameter. The nested line turns out to be less demanding in the sense of dimensions, but its ITER-compatible implementation may turn out to be more complex.

A coil-based RF decoupler, as discussed in Appendix III, may also be considered alternatively to a "metallic insulator."

4) Topology Parameters of the Planar RF Prematcher Verification by Finite Element Simulation: The validity of the RF prematcher parameters calculated using the electrostatic approximation was verified by the full-wave FEM simulation. The coupled thermal-electric problem was simulated for the structure depicted in Fig. 8, and the simulation parameters are listed in Table III. These simulations show [see Fig. 12(a)] that at the frequency f_0, the planar RF prematching circuit provides a maximum P_L in the range of Z_L values that are close to, but not equal to the initially estimated target values.

This discrepancy illustrates the drawback of the electrostatic approximation, which fails to account for all of the effects associated with the RF electromagnetic field distribution in a 3-D structure. To avoid this inconsistency, an RF prematcher topology should be synthesized using full-wave simulation/optimization, taking into account also the elements interfacing with the prematcher. It is essential as well to analyze the RF prematcher tolerance to the Z_L variation depending on the discharge operating point.

TABLE III
THERMAL-ELECTRIC SIMULATION PARAMETERS

Parameter	Value	Comment
Load impedance range bounding points Z_L (Ω)	(2-j2); (2-j20); (20-j2); (20-j20)	See Fig. 3 for the experimental data on the ~100x100 mm 55.G6 mirror M1
Frequency f_0 (MHz)	80	Assumed optimal for mirror cleaning selectivity [9]
Forward RF power P_F at the pre-matcher input (W)	500	Worst-case estimation for a DC-coupled scheme, assuming the power of 1-2 W/cm^2 absorbed in the plasma [18], and considering RF loss in the pre-matcher
Ambient and initial temperature T_a, T_0 (°C)	100	Fair assumption, based on ITER policies [48, Sec. 4.3.2.1]
Dielectric loss tangent tan δ (unitless)	10^{-2}	Worst-case assumption for the neutron irradiated AlN [49]
Dielectric thermal conductivity k (W.m^{-1}.K^{-1})	30	
Relative dielectric permittivity ε_r (unitless)	9	AlN dielectric assumed [50]
Surface emissivity a (unitless)	0.2	Assumption for a polished ceramic surface

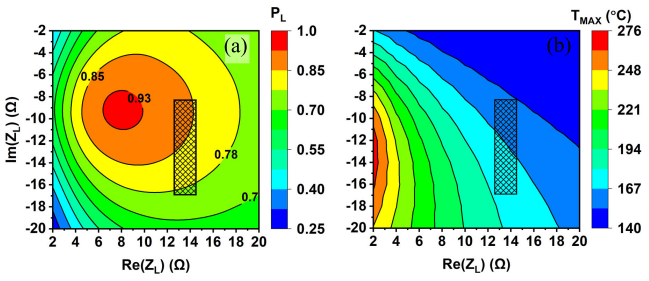

Fig. 12. Results of the planar RF prematcher thermal-electric FEM simulation in dependance on load impedance Z_L. (a) Load power P_L. (b) Maximum board temperature T_{MAX}.

The maximum steady-state prematcher board temperature T_{MAX} in the region of the highest P_L values is of 160 °C–210 °C [see Fig. 12(b)], with a temperature gradient of no more than 5 C*cm^{-1} over the entire Z_L variation range. Interestingly, there is no direct correspondence between the T_{MAX} and P_L profiles.

IV. STRUCTURAL DESIGN STUDY OF THE PLANAR RF PREMATCHING DEVICE

Following the ideas outlined above, the design of an FMU with an RF power distribution system should address two major problems: assuring the spatial stability of optical surfaces and the structural integrity of ceramic parts. The optical stability problem is being resolved separately study and is not considered in this study.

For ceramic parts, the following failure risks have been identified: 1) expansion due to external thermal cycling; 2) internal RF power loss; 3) swelling produced by neutrons; and 4) cracking caused by inertial impacts from electromagnetic or seismic events.

The limiting mechanical properties of ceramics are established by probabilistic parameters and degrade with neutron irradiation. Therefore, the stresses on the ceramic elements should be kept as low as possible to the strength limits to ensure their structural integrity. It is also desirable that the partial destruction of the ceramic part without its removal from the assembly volume does not result in the complete failure of the entire assembly. It is known that the compressive strength of ceramic materials is times higher than their bending, shearing, and tensile strengths [51]. As a result, the design must ensure the action of predominantly compressive forces on the ceramic parts.

The choice of AlN as a dielectric in the RF prematching unit and RF decoupler was based on [49], which investigated the degradation of RF and mechanical properties of several types of ceramics under the action of neutrons. Other candidates include Si_3N_4, which has a lower dielectric permittivity, and ZrO_2, which has the highest mechanical strength, as well as a very high dielectric constant $\varepsilon_r \approx 27$. This enables ZrO_2 for the use in situations where increased mechanical loads act, i.e., as insulating elements in mirror-electrode fastening, or where a significant reduction in electrical length is required.

Planar topology can be implemented either with commercially available ceramic plating technologies such as novice transient liquid phase bonding [52], traditional direct bond copper (DBC) [53], active metal brazing (AMB) [54], thick printed copper (TPC) [53], [55], or by simply folding a metal foil between the ceramic plates. Consideration should be given to the durability of the metallization layer under thermal cycling and neutrons, as well as to the effect of the metallization process on the strength of ceramics [56]. The DBC and AMB processes cause an interface layer between ceramics and metal that can be tens of micrometers thick and exhibit semiconductor characteristics, resulting in extra RF power loss and subsequent structure heating. The low-temperature co-fired ceramics (LTCC) technology [57], [58], and the idea of replacing a ceramic board with one created utilizing aluminum deep oxidation technology [59] are both potentially interesting. However, their application to the ITER in-vessel environment is yet unclear.

A. Fastening Principle for Ceramic Parts, Ensuring Structural Integrity Under Mechanical, Thermal, and Neutron Loads

Fig. 13(a) shows a schematic of the ceramic fastening, which compensates for thermal, neutron, and inertial loads. The ceramic plates 4 are supported with a snug fit by base plates, milled on surfaces A and B of the steel housing 1.

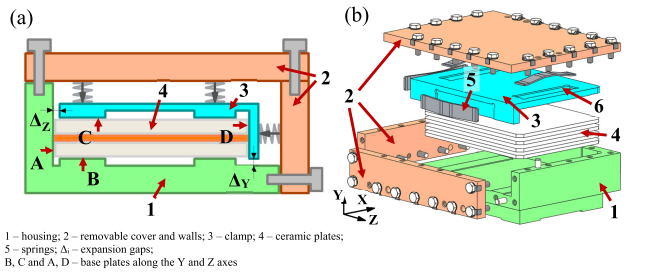

Fig. 13. Ceramic parts fixation in the FMU prematcher. (a) Schematic (*YZ* view). (b) Exploded view of the FMU RF prematcher design.

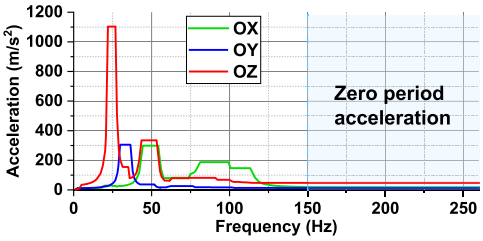

Fig. 14. VDE II response spectra at the FMU mounting points (see Fig. 1 for axes direction).

Clamp 3 provides nondeforming pressing of the ceramic parts to the base plates, while the base plates are also machined on surfaces C and D. Cover 2 with preloaded springs 5 closes the force loop, providing pressing and fixing ceramic parts in three orthogonal directions. The snug fit of the ceramic plates to each other and to surface A–D is critical to ensuring the best performance of this fastening principle. Therefore, all of the surfaces in the force loop must meet a high shape tolerance.

Other important considerations include selecting the proper springs preload and expansion gap Δ between the clamp and the housing. On the one hand, the fixation of ceramic parts must be sufficiently rigid to prevent their fracture as a result of separation with subsequent collision during inertial impacts. On the other hand, it must be flexible enough to avoid fracture owing to overstress caused by thermal expansion or swelling. Since these requirements contradict, there is some optimal spring preload.

Both the spring preload and the minimum Δ values were quantified, using the estimate of the forces, acting on the structure under inertial and thermal loads. This assessment was performed for an RF prematching device based on four stacked ceramic plates with realistic dimensions of $105 \times 80 \times 10$ mm.

B. Summary of Neutron, Thermal, and Inertial Loads

The total neutron fluence estimation at the FMU location was based on the MCNP simulation results available for the Equatorial port EQ#11 [60, Table 2], since the environment in port EQ#17 is similar. Total neutron fluence of $\sim 1.7 \times 10^{20}$ cm^{-2} was estimated according to the SA-2 scenario [61] by multiplying the revealed neutron flux of $\sim 10^{13}$ cm$^2 \cdot$ s^{-1} at the FMU location by the total D-T fusion phase duration of 1.7×10^7 s (i.e., 4700 h).

An estimate of ~0.5% swelling linear expansion of the ceramic parts at the aforementioned fluence was made using the data from [62, Fig. 6]. A decrease in flexural strength from 360 to 270 GPa and in thermal conductivity from 170 to 30 W·m^{-1}·K^{-1} was reported [63] for AlN.

The estimated fluence turns out to be close to the microcracks onset threshold of 8×10^{20}–2×10^{21} cm^{-2}. Microcracking occurs along ceramic bulk grain boundaries due to the anisotropy of swelling, which entails a more pronounced further degradation of the ceramic properties and observed discrepancy between microscopic and macroscopic volume change [62]. Annealing at 200 °C–1300 °C is known to partially restore the dimensions of the swollen ceramics [64], [65], [66].

Depending on the port location and the distance between the FMU and the fusion plasma edge, the neutron heating power density at the FMU location ranges from ~0.3 to 1 W·cm^{-3} in the fusion plasma operation (FPO) mode [61, Table 4]. Additionally, a heat flux will act on the surfaces in line of sight of the plasma, originating from radiation and charge exchange from plasma. The intensity of this heat flux on the DFW surfaces facing the plasma is estimated at 35 W*cm^{-2} [67], [68]. However, depending on the system location and viewing factors, it can be significantly attenuated when passing through the diagnostic channel in the DFW. For example, [69] reports a power of 5 W, almost uniformly distributed over the surface of a 150 × 60 mm mirror [70] with an input aperture of ~Ø10 mm. Taking these considerations into account, the range of this flux can be estimated as of ~10^{-4}–1 W*cm^{-2}.

In the Baking mode, the port walls will be heated up to 200 °C–240 °C, and conductive heating of all structures inside the port should be ensured to the same temperature. In the FPO mode, the port wall temperature is maintained at ~70 °C.

The mirror cleaning system is not intended to operate in these two modes, so it will not self-heat due to internal RF loss. However, the FMU must survive these states without damaging the ceramic parts, as well as maintain the optical surfaces in their proper positions.

The above FEM estimate of the loss in the RF prematcher during the cleaning system operation predicts a volumetric release of 5%–7% of the input power. With an input power of 500 W, such a loss will amount to ~35 W. The remaining power is distributed between the mirror surfaces and the FMU walls by ion and electron bombardment, as well as optical emission caused by inelastic collisions in the RF discharge plasma.

To summarize, a reasonable limit of the FMU structures heating in any operating mode of <280 °C–300 °C can be assumed. Temperature gradients should be carefully considered throughout the detailed FMU design, as the ceramic attachment is sensitive to uneven spring loading.

The highest inertial loads are expected during the electromagnetic event vertical displacement event (VDE II) [71]. Fig. 14 depicts the acceleration response spectra for all three port axes in this loading scenario.

The first eigen frequency of the RF prematching device structure, revealed from the FEM simulation, appeared of 4021 Hz. This is significantly higher, than the zero-period acceleration (ZPA) cut-off frequency for the given response

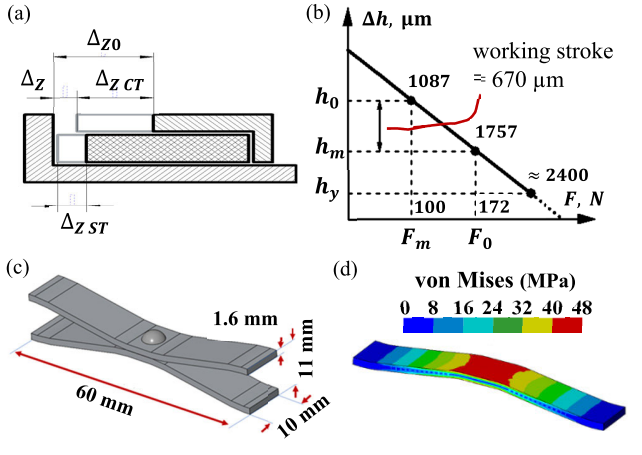

Fig. 15. Assessment of the Δ_Z gap and spring parameters. (a) Influence of the clamp/ceramic stack expansion on the change in Δ. (b) Force characteristic of the spring. (c) Geometric configuration of the spring. (d) Stress distribution in the spring compressed to h_m.

spectra. At the first eigen frequency, in the case it is higher than the ZPA cut-off frequency, the structure moves like a rigid body with ZPA, without any inertial effects [72, Sec. 4.2]. Such a high value of the first eigen frequency is ensured by the high structure rigidity: the structure is compact and has sufficiently rigid fastenings.

The maximum ZPA value of 47 m*s^{-1} (∼5 g) applies along the port *Z*-axis. The stress acting on the plates under the inertial loads can be quantified by estimating the stress-strain state of the RF prematching unit under an equivalent static load equal to the maximum ZPA. An equivalent static load of 10 g is assumed conservatively in the further estimations.

C. Choosing the Expansion Gap Δ and Spring Parameters

The expansion gap Δ is determined by the difference between the elongation of the clamp due to thermal expansion and the elongation of the ceramic plates caused by thermal expansion and swelling. The spring parameters are determined by the required pretension and by the oscillating mass, comprised of the clamp and the stack of ceramic plates.

The gap and spring characteristics are estimated for the *Z*-axis as the most indicative, since the highest elongations and inertial loads act along it. The gap Δ_Z shrinks as the temperature rises since the metal elongates more than the ceramic. On the contrary, Δ_Z increases under the action of neutrons since the ceramic swells significantly while the metal almost does not swell. To keep the device operable, the gap should remain nonzero: $\Delta_Z = \Delta_{Z0} + \Delta_{ZS} - \Delta_{ZC} > 0$, where Δ_{Z0}—initial gap at 20°C when the ceramic is not swelled, $\Delta_{ZS} = 145$ μm—absolute thermal elongation of the ceramic plates stack heated from 20 °C to 320 °C, and $\Delta_{ZC} = 533$ μm—absolute thermal elongation of the clamp [see Fig. 15(a)].

Choosing $\Delta_{Z0} = 500$ μm, we get $\Delta_Z(320\ °C) = 500 + 145 - 533 = 112$ μm. The maximum operating temperature at which the equality $\Delta_{ZC} = \Delta_{Z0} + \Delta_{ZS}$ is fulfilled is 387 °C. The residual gap $\Delta_Z(320\ °C)$ can be increased by selecting a larger Δ_{Z0} value. However, this should be done carefully, because a large thickness of ceramics, not covered by the clamp, can lead to the RF power leakage with following decrease in the device efficiency. A parasitic RF discharge may also appear in the spring cavity.

For the spring parameters assessment, the oscillating mass of 1 kg is assumed, considering a ∼30% safety margin. Therefore, a force of 100 N will act on the spring under an inertial load of 10 g, which should be countered by the spring pretension force under some initial compression h_0. The maximum spring compression, corresponding to the maximum expansion of ceramics (expansion of the metal can be neglected in the first approximation) is $h_m = h_0 + \Delta_{ZS} + \Delta_{ZSN} = 1757$ μm, where $\Delta_{ZSN} = 525$ μm represents the swelling of ceramic plates. The spring shape and material should be chosen so that the maximum compression h_m is less than h_y, which corresponds to the spring material yield strength. A suitable spring material for this application is 660 grade steel, which has a yield strength of 671 MPa at 100 °C [73, Table 2]. For the feasibility reasons, a minimum spring stiffness should be sought. From this position, it seems optimal to use a stack of two flat springs, which force characteristic is shown in Fig. 15(b). The working stroke of such a springs stack is 1313 μm, which exceeds the required stroke of $\Delta_{ZS} + \Delta_{ZSN} = 670$ μm. The spring design is depicted in Fig. 15(c). The maximal compressive stress at the h_m tension is of 480 MPa, resulting in a yield strength margin of 1.4. A more accurate calculation of the spring characteristics should be performed, taking into account the refined device parts elongation under the realistic temperature distribution, as well as the temperature dependency of the materials parameters.

D. Strength Evaluation of Ceramic Plates Under the Inertial Impact

Ceramics are classified as brittle materials, with their strength determined by fracture toughness and the characteristic size of inevitably present flaws such as voids, foreign inclusions, grain size inhomogeneities, and surface and volume microcracks. The crack growth rate is determined by the so-called stress intensity factor: $K_I = \sigma Y (a_m)^{1/2}$ (2), where $2a_m$—length of largest crack, σ—acting stress, Y—shape factor, characterizing the shape, size, and location of the cracks [74, eq. (2.55)].

Fig. 16(a) shows the distribution of maximum principal stress σ_1 in the stack of loaded ceramic plates, revealed from the FEM simulation. Positive values of σ_1 correspond to tensile stress, while negative values indicate compressive stress. As mentioned above, we are primarily interested in the positive values of σ_1, since ceramic resists tension worse than compression [75, Section 19.6].

The maximum tensile stress in the ceramic plates $\sigma_{1\max} \approx 2$ MPa occurs in the contact zone with the base plates. Assuming the maximum random initial crack size for ground AlN parts $2a_m \approx 100$ μm [76], we estimate K_I and the crack growth rate under the action of $\sigma_{1\max}$. Since the maximum stress is localized on the plates surface, the surface crack is estimated with the shape factor Y, determined by the following

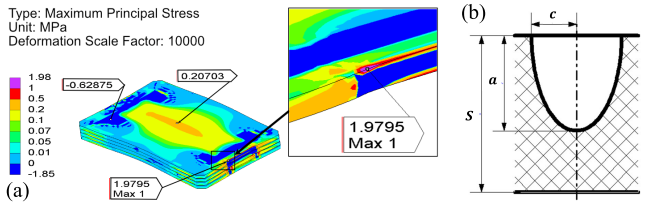

Fig. 16. Ceramic plates stack strength FEM estimation. (a) Maximum principal stress σ_1 distribution. (b) Surface semi-elliptical crack parameterization [illustration to (2)].

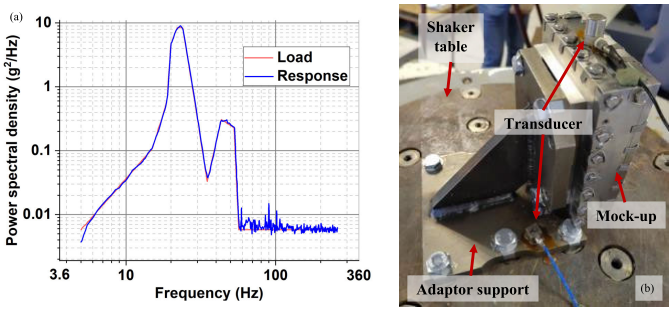

Fig. 17. Vibrational test of the ceramic plates fastening the planar RF prematcher. (a) Applied impact corresponding to a VDE II event in ITER port vertical direction. (b) Mock-up with vibration transducers installed on the i250/SA5M shaker.

expression [see Fig. 16(b)]:

$$Y = \frac{(2 - 0.82a/c)\gamma}{\left[1 - \left(0.89 - 0.57\sqrt{a}/c\right)^3 (a/S)^{1.5}\right]^{3.25}} \approx 1.3 \quad (2)$$

where $\gamma = [1.1 + 0.35(a/S)^2](a)^{1/2}/c, a = 50$ μm—the minor semi-axis of an elliptical crack, c the—major semi-axis (estimated as $c = a$), and $S = 2.5$ mm is the thickness of a single ceramic plate (for simplified form, see [74, Fig. 2.19]). The estimated $K_I = 0.018$ MPa$*m^{(1/2)}$ is much lower than the critical value $K_{\mathrm{IC}} \approx 3.2$ MPa $* m^{(1/2)}$ for AlN [77]. A typical dependence of the crack growth rate v on K_I for ceramic materials has a "slow growth" threshold K_{I0} [78], which occurs at very low crack growth rates of $v_0 \lesssim 10^{-10}$ m*s^{-1}. The experimental data on $v(K_I)$ for AlN [77, Fig. 9] shows $v_0 = 1.5{\cdot}10^{-11}$ m/s at $K_{I0} = 2.8$ MPa $* m^{(1/2)}$. For the case under consideration, $K_I \ll K_{I0}$, thus crack growth rate turns out to be negligible (much lower than v_0). Thus, the proposed ceramic plates fastening scheme provides K_I value for AlN plates ~100 times lower than those that onset crack growth.

V. Pilot Experimental Verification of the Planar RF Prematcher

A. Vibrational Test of the Ceramic Plates Fastening

The resistance of the proposed ceramic plate fastening was confirmed by a vibration test of the RF prematching device mass-dimensional mock-up [see Fig. 13(b)]. The worst-case broadband random vibration spectrum [see Fig. 17(a)] corresponding to the VDE II event (see Fig. 14) was applied to the mock-up along the Z-axis (see Figs. 1 and 3).

Prior to the main test, the frequency response of the mock-up assembly and adaptor support depicted in Fig. 17(b) was measured in the 5–1000 Hz range using a low-signal sinusoidal sweep. The measurements revealed the eigen frequencies of the support in the range of 500–600 Hz, which is consistent with preliminary FEM simulations. The mock-up itself had no eigen frequencies in the swept range, indicating that the proposed ceramic fastening design is sufficiently rigid for the use in ITER.

The primary impact was applied for 30 min. The following visual inspection revealed no chips, cracks, or other flaws on the ceramic plates.

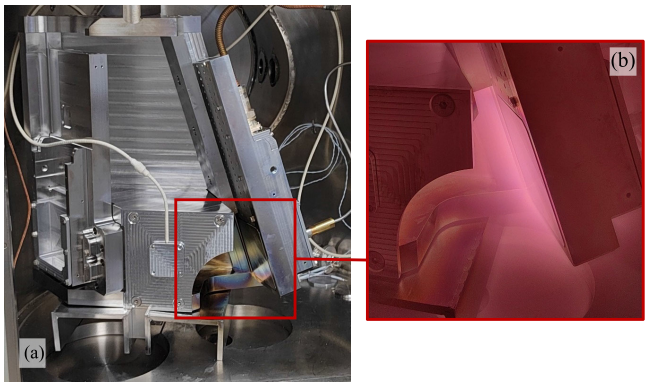

Fig. 18. 55.G6 FMU full scale mock-up. (a) Installed inside the vacuum chamber. (b) Mirror M1 cleaning with an 80 MHz Ar RF discharge at 3 Pa, 150 W.

B. RF Performance of the Planar RF Prematching Device

The performance of the planar RF prematching device was checked experimentally as part of the built 55.G6 system FMU mock-up (see Fig. 18).

Fig. 19(a) depicts the power reflection coefficient $|\Gamma|^2$ at the system input with RF prematching, measured for He RF plasma in the pressure range of 1–10 Pa and RF power range of 50–300 W for the discharge circuit with DC decoupling. With a fixed setting of the prematching device LC elements, the $|\Gamma|^2$ value did not exceed 5% across all operating points. The precise $|\Gamma|^2$ minimum for each operating point was achieved by a slight adjustment of the operating frequency f_T. Tuning was made between 79.3 and 84.1 MHz [see Fig. 19(c)], which is of ~5% of the base frequency of 80 MHz. This has little effect on mirror cleaning effectiveness, and can be used to improve the RF cleaning of diagnostic mirrors in ITER. The optimal frequency f_T is clearly dependent on pressure for both gases, while the dependence on input power is much less pronounced.

It should be noted that the best $|\Gamma|^2$ values were achieved after some adjustment of the prematcher conductors' topology, compared to the initially calculated and fabricated one. This confirms the justification for using the full-wave 3-D simulation for topology synthesis, as well as highlights the need to develop a prematcher initial adjustment technique.

For the Ar discharge, with the same prematcher setting, the maximum $|\Gamma|^2$ value reached 33%, which is explained by the shift of Z_L variation region due to a gas change.

The negative DC self-bias U_{BIAS} of minus 100–120 V occurred on the mirror-electrode for He discharge in the RF power range of ~50–150 W [see Fig. 19(b)], corresponding

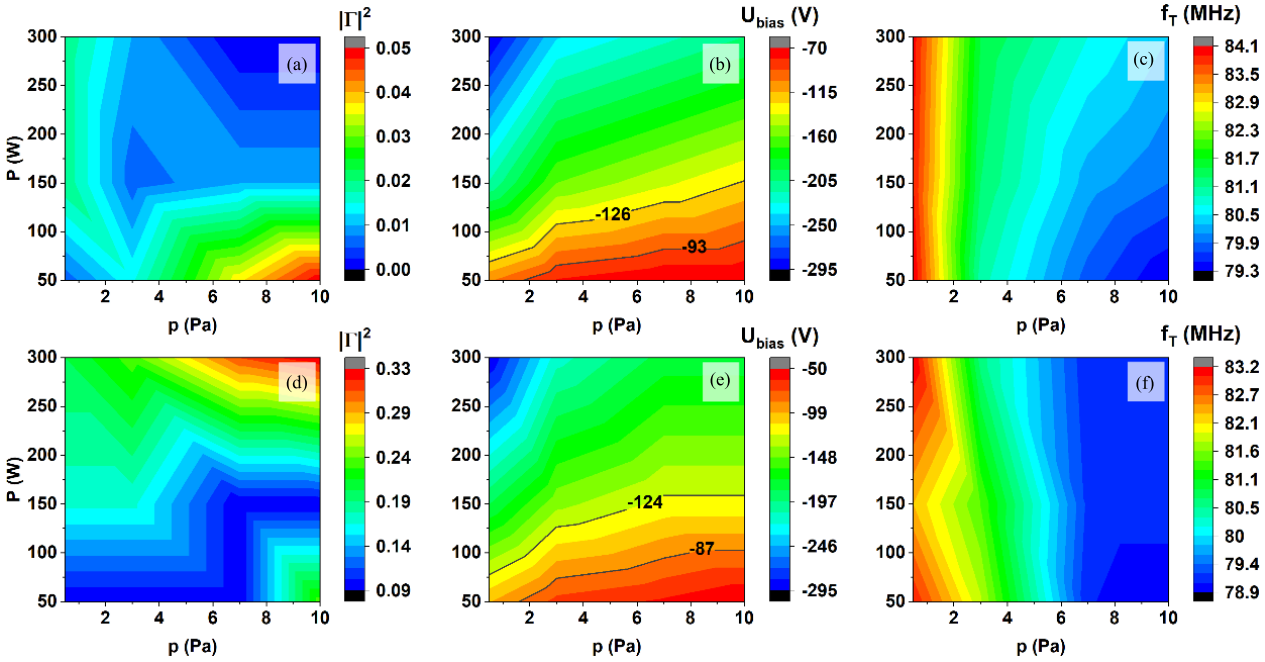

Fig. 19. Results of the pilot experiment with planar RF prematching device with (a)–(c) He and (d)–(f) Ar discharge in dependence on RF power and gas pressure. (a) and (d) RF power reflection coefficient $|\Gamma|^2$. (b) and (e) RF electrode self-bias U_{BIAS}. (c) and (f) Frequency f_T at which the best RF matching achieved.

to the power density of 0.5–1.5 W·cm^{-2}. The position of the maximum of the energy distribution function of ions bombarding the mirror-electrode under the considered discharge conditions will be ∼30 eV higher than the absolute value of the observed U_{BIAS} [13]. This energy range appears advantageous since the sputtering yield of the FM materials (Mo or Rh) by He ions is substantially lower than that of Be or B [79], [80], which are the primary anticipated components of mirror contaminating deposits.

This allows for minimal damage to the mirror [12] while maintaining a suitable cleaning rate of 1–10 nm/h [15], [81]. Similar U_{BIAS} values were achieved for Ar [see Fig. 19(e)].

With an ex-vessel RF matching device used instead of the prematcher, the U_{BIAS} value never dropped below −30 V under the same experimental conditions, indicating a low power supplied to the RF discharge. As pointed out in Section III, the missed power was likely dissipated in the ∼40 cm long in-vessel RF feeder segment (RG-213, LCF78-50 or MI cable PK316 50-3-71) that connected the mirror-electrode to the ex-vessel RF matching device. Excessive power dissipation in the RF feeder was confirmed in this scenario by its rapid heat up, whereas no overheating occurred when the prematcher was in place.

VI. Conclusion and Outlook

A study of the design principles of the FMU of an ITER optical diagnostic system, equipped with cooled mirrors and a mirror cleaning system, utilizing a local RF discharge, is proposed on the example of the 55.G6 system. The RF discharge load impedance is recognized as a major design input, along with reflecting surfaces shape and spatial position.

It is demonstrated that a passive preliminary RF matching circuit, located directly adjacent to the mirror electrode, increases the amount of RF power delivered to the RF discharge while notably reducing the power dissipation and heat load in the feeder in-vessel section. This prematching device appears to be a novel approach to RF plasma technology systems, although it does raise some design challenges.

Analysis of a prematcher, based on ITER-compatible 50 Ω MI cable segments revealed, that a single stub in parallel to the load is applicable to a limited range of load impedances. A prematcher, based on L-shaped MI cable stubs, may appear as compromise solution for systems with small mirrors, with the overall RF power budget split between loss in the stubs and RF discharge load.

Implementing RF prematcher, whether planar or based on MI cable stubs, requires the development of an initial adjustment process.

Three options for mirror cooling manifold implementation that provide mirror-electrode RF decoupling from a grounded housing are explored. An approach to choosing their optimal geometric parameters is described, which helps to minimize their influence on the RF discharge, while retaining minimal dimensions. An RF-decoupler in the form of a quarter-wave "metallic insulator" is preferred over an inductive low-pass filter at ∼80 MHz. While both devices have comparable dimensions, a coil self-resonance in the 40–120 MHz range is particularly sensitive to dimensions and material properties, complicating design and tuning. Further enhancements to the RF prematcher and RF decoupler are underway to reduce their size. Utilizing RF decoupler length as a degree of freedom for initial adjustment, in conjunction with RF prematcher circuit layout, is one of the promising ways for such dimensions minimizing.

An approach is being developed that applies full-wave RF simulation to synthesize a planar RF prematcher topology,

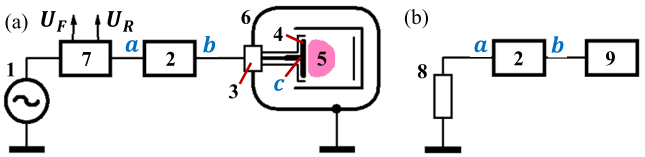

1 – RF power source; 2 – RF matching unit (together with the DC-break unit in case of DC-decoupled scheme); 3 – vacuum RF feedthrough with in-vessel feeder section; 4 – RF electrode; 5 – RF discharge plasma; 6 – vacuum chamber; 7 – RF reflectometer, 8 – reference RF load; 9 – Vector Network Analyzer. Points: a – RF matching unit input; b – RF matching unit output; c – RF electrode connection point.

Fig. 20. Measuring the capacitive RF discharge impedance by the substitution method. (a) and (b) Schematic for step 1 and step 2.

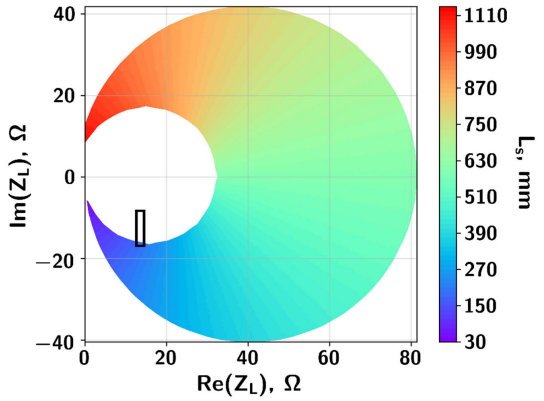

Fig. 21. Range of load impedance values which can be matched at 80 MHz using a parallel shorted stub of 50 Ω MI cable.

as well as to analyze of the effect of load impedance deviations and circuit design features on the efficiency of the RF power delivery to the discharge.

Pilot experiments were carried out to demonstrate the RF performance and structural integrity of the ceramic components of the planar RF prematcher designed utilizing the described principles. The details of the corresponding experimental campaign will be described in a further article.

The principles of fastening the mirror-electrodes are being developed to ensure reflecting surface shape and spatial position stability within required tolerances as well as electrical isolation from the grounded housing. The requirements for shell enclosure shape optimization will be primarily addressed to prevent redeposition on mirrors and mitigate local nonself-sustaining RF discharges.

Appendix A
RF Load Impedance Measurement

The load impedance Z_L was measured with a two-step substitution method as follows. On the first step [see Fig. 20(a)], having set the RF discharge (5) operating point (f, W, p ...), the reflected wave is minimized by adjusting the matching unit (2) to minimize U_R observed at the reflectometer (7) output.

The residual reflection of $U_R/U_F \lesssim 0.1$ is acceptable. On the second step [see Fig. 20(b)], the matching unit (2) is disconnected from both the vacuum chamber (6) and the RF power source (1), while its settings are kept unchanged. The reference RF load (8) is then connected to the point a, while the vector network analyzer (9, VNA) is connected to the point b for measuring the complex impedance value Z_M. Following the substitution principle, the impedance Z'_L of the in-vessel RF feeder section (3) together with Z_L is a complex conjugate to Z_M. Finally, Z'_L is reduced to the electrode (4) connection at the point c and hence to Z_L.

The need to reswitch the circuit with each measurement may lead to a significant scatter of results by the substitution method. Hence, the actual region of impedance variation may appear even narrower. There are alternative in situ impedance measurement methods like directional couplers or VI-probes, which do not require circuit reswitching. However, these types of instruments possess their own types of uncertainties, which may result in comparable or even higher measurement errors. An alternative way of RF discharge impedance measurement [82], also employing substitution principle, is used in [30]. However, as in this case, error analysis for it is unknown.

It seems, that for the practical purpose of developing an RF prematching system, the relative change in Z_L is more important than its absolute value. Therefore, the best value of experimental data can be achieved by measuring the relative change in Z_L using some in situ method, with absolute referencing by the substitution method at several operating points.

Appendix B
RF Prematcher Based on MI Cable Stubs

The circuit input impedance with a single-stub prematcher [see Fig. 7(a)] is expressed as $Z_{\text{IN}} = Z_{TL}Z_L/(Z_{TL} + Z_L)$. Fig. 21 illustrates the range of Z_L real and imaginary parts, at which the power reflection coefficient $|\Gamma|^2 = |(Z_{\text{IN}} - 50)/(Z_{\text{IN}} + 50)|^2$ remains below 0.05. The color scale indicates the physical length L_S of a short-circuited coaxial MI cable stub, required to achieve corresponding impedance Z_{TL} at 80 MHz, which in turn is determined according to (1).

A single stub appears insufficient to match the whole Z_L region P_1, ..., P_4 in Fig. 3(c), since the matching range is only partially overlapped with the target. The matching range can, however, be shifted by choosing another stub Z_0 via a nonstandard MI cable.

A larger matching capability is provided by an L-shaped circuit with two MI cable stubs. Fig. 22(a) shows where $|\Gamma|^2 < 0.05$ for points P_1, ..., P_4 in dependence on each stub TL_1 and TL_2 length (L_{S1} and L_{S2}, respectively). Fig. 22(b) shows the corresponding matching circuit power balance.

Appendix C
Coil-Based RF Decoupler

A widespread method of RF decoupling of cooled components in technological facilities utilizes coil-twisted cooling manifolds connected in parallel with the load. The example circuit in Fig. 23(a) contains a load impedance Z_L, an inductive RF decoupler Z_F, and a prematcher L-circuit, configured and tuned according to Section III-B. Fig. 23(b) shows the power balance in the circuit versus the coil inductive reactance $X_F = \text{Im}(Z_F)$. The coil quality factor of 200 is assumed.

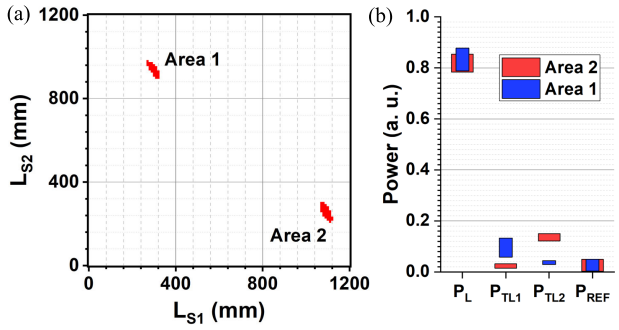

Fig. 22. Performance of an L-shaped prematching circuit based on 50 Ω MI coaxial cable stubs. (a) Stub lengths for $|\Gamma|^2 < 0.05$. (b) Circuit power balance.

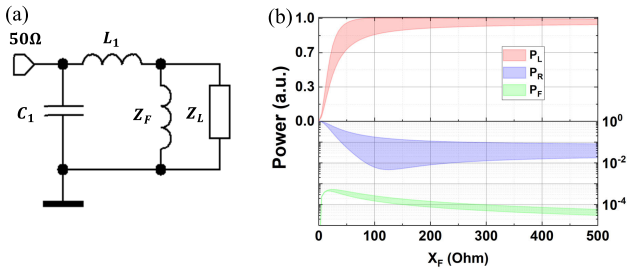

Fig. 23. Coil-based RF decoupler. (a) Circuit schematic. (b) Circuit power balance.

At $X_F > 500$ Ω, the minimal P_L becomes >90%, while at $X_F > 1.8$ kΩ the difference between minimal P_L power value and its value at $X_F \to \infty$ approaches 1%.

To evaluate the feasibility of an inductive decoupler, consider $X_F = 500$ Ω as a reasonable compromise between its dimensions and efficiency. Since RF decoupling is required for both the input and output tubes, and the coils appear to be connected in parallel, the value of each should be doubled. In the estimates below, the minimum DN6 tube with an outer diameter of 10.2 mm is considered [47]. To mitigate parasitic interaction with surrounding structures and suppress RF breakdown, it is desirable to enclose the coil with a conductive shield and fill the interior volume with a solid dielectric.

Coil parameters were computed using Coil64 v1.2.12 software with further FEM correction for self-resonance. The X_F growth rate increases sharply as the frequency approaches the parallel self-resonance, which turns out to be the first, while it changes the sign behind the resonance, rendering the prematching circuit of the selected structure inoperable. Unfortunately, it was not possible to find the coil parameters that provide X_F far from the self-resonance, since increasing the turns count t shifts the self-resonance below the operating frequency, and decreasing it reduces X_F unacceptably. Table IV lists a compromise coil parameter set when the operating frequency was close to resonance on the inductive branch, but with sufficient tolerance in coil parameters to prevent qualitative change in the input impedance.

Fig. 24 depicts a sketch of the coil-based RF decoupler and its frequency response as derived from FEM simulations. A sensitivity analysis revealed that changing the winding

TABLE IV
RESULTING PARAMETERS OF THE 80 MHZ COIL-BASED RF DECOUPLER

Turns count t	2.1
Inner diameter (mm)	50
Pitch (mm)	20
Clearance to housing (mm)	10
Dielectric filling ε_r	3.8 (quartz)
Weight (kg)	~0.7 (including water)
Winding length (mm)	~60

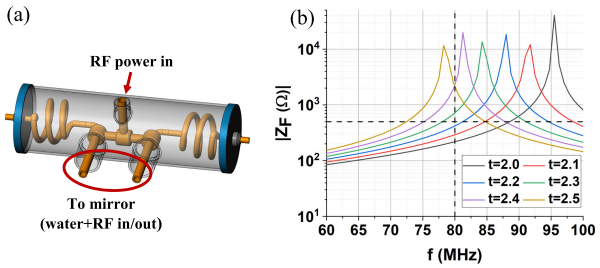

Fig. 24. (a) Conceptual design of the coil-based RF decoupler. (b) FEM-simulated coil frequency response.

pitch or coil radius by ~0.1 mm leads to a satisfactory change in coil absolute impedance $|Z_F|$ by ~10–20 Ω. Quartz was used as having the lowest permittivity $\varepsilon_r = 3.8$ among ITER-compatible solid dielectrics. The grounded shield already has no meaningful effect when the gap is of >4–5 mm. The springiness of the solenoid will require special attention during detailed development to ensure that the coil dielectric cover is structurally stable against inertial loads.

Nested tubes can minimize the needed coil inductance while increasing the resonance frequency. However, structural implementation of this kind of solenoid is thought to be problematic. The use of a coil-based RF decoupler in this particular FMU design appears to be difficult owing to self-resonance and issues in preventing RF breakdown.

ACKNOWLEDGMENT

The views and opinions expressed herein do not necessarily reflect those of the ITER Organization.

REFERENCES

[1] E. E. Mukhin et al., "Perspectives of use of diagnostic mirrors with transparent protection layer in burning plasma experiments," in *Proc. AIP Conf.* Varenna, Italy: AIP, 2008, pp. 365–369, doi: 10.1063/1.2905100.

[2] G. De Temmerman et al., "Beryllium deposition on international thermonuclear experimental reactor first mirrors: Layer morphology and influence on mirror reflectivity," *J. Appl. Phys.*, vol. 102, no. 8, Oct. 2007, Art. no. 083302, doi: 10.1063/1.2798389.

[3] D. Samsonov et al., "Large-scale collecting mirrors for ITER optical diagnostic," *Nucl. Fusion*, vol. 62, no. 8, Aug. 2022, Art. no. 086014, doi: 10.1088/1741-4326/ac544d.

[4] A. Rogov and Y. Kapustin, "Development of the plasma cleaning system for the entrance mirror of the CXRS-edge diagnostics of ITER on the basis of a discharge with a mesh hollow cathode," *Instrum. Express Tech.*, vol. 64, no. 3, pp. 393–400, 2021, doi: 10.1134/S0020441221030313.

[5] E. E. Mukhin et al., "First mirrors in ITER: Material choice and deposition prevention/cleaning techniques," *Nucl. Fusion*, vol. 52, no. 1, Jan. 2012, Art. no. 013017, doi: 10.1088/0029-5515/52/1/013017.

[6] G. D. Loesser et al., "ITER diagnostic first wall," *Fusion Sci. Technol.*, vol. 64, no. 2, pp. 156–160, Aug. 2013, doi: 10.13182/fst12-558.

[7] C. S. Pitcher et al., "Port-based plasma diagnostic infrastructure on ITER," *Fusion Sci. Technol.*, vol. 64, no. 2, pp. 118–125, Aug. 2013, doi: 10.13182/fst13-a18065.

[8] A. Kobelev et al., "Collisional RF sheath in capacitive discharge in strong oblique magnetic field," *Phys. Plasmas*, vol. 26, no. 1, Jan. 2019, Art. no. 013504, doi: 10.1063/1.5051314.

[9] A. M. Dmitriev et al., "In situ plasma cleaning of ITER diagnostic mirrors in noble-gas RF discharge," *Phys. Scripta*, vol. T170, Dec. 2017, Art. no. 014072, doi: 10.1088/1402-4896/aa95e5.

[10] F. Leipold et al., "Cleaning of first mirrors in ITER by means of radio frequency discharges," *Rev. Scientific Instrum.*, vol. 87, no. 11, Nov. 2016, Art. no. 11D439, doi: 10.1063/1.4962055.

[11] M. De Bock, F. Leipold, R. Reichle, and C. Vorpahl, "Memorandum on diagnostic mirror cleaning regime," ITER IDM, Saint-Paul-lez-Durance, France, Tech. Rep. ITER_D_T3B5C5, v1.1, 2016.

[12] J. Peng et al., "Sputtering tests of single crystal molybdenum and rhodium mirrors at high ion fluence for in situ plasma cleaning of first mirrors in ITER," *Fusion Eng. Design*, vol. 128, pp. 107–112, Mar. 2018, doi: 10.1016/j.fusengdes.2018.01.061.

[13] L. Moser et al., "Investigation and plasma cleaning of first mirrors coated with relevant ITER contaminants: Beryllium and tungsten," *Nucl. Fusion*, vol. 57, no. 8, Aug. 2017, Art. no. 086019, doi: 10.1088/1741-4326/aa73e2.

[14] F. Sanchez et al., "Surface modification of ITER-like mirrors after one hundred cleaning cycles using radio-frequency plasma," *J. Nucl. Mater.*, vol. 581, Aug. 2023, Art. no. 154382, doi: 10.1016/j.jnucmat.2023.154382.

[15] A. Ushakov et al., "Removing W-contaminants in helium and neon RF plasma to maintain the optical performance of the ITER UWAVS first mirror," *Fusion Eng. Design*, vol. 136, pp. 431–437, Nov. 2018, doi: 10.1016/j.fusengdes.2018.02.082.

[16] L. Marot et al., "RF discharge mirror cleaning for ITER optical diagnostics using 60 MHz very high frequency," *Fusion Eng. Design*, vol. 163, Feb. 2021, Art. no. 112140, doi: 10.1016/j.fusengdes.2020.112140.

[17] L. A. Varshavchik et al., "Three-dimensional simulation of neutral transport in gases and weakly ionized plasmas," *Plasma Phys. Controlled Fusion*, vol. 63, no. 2, Feb. 2021, Art. no. 025005, doi: 10.1088/1361-6587/abca7e.

[18] A. M. Dmitriev et al., "RF plasma cleaning of water-cooled mirror equipped with notch filter based on shorted $\lambda/4$ line," *Fusion Eng. Design*, vol. 146, pp. 1390–1393, Sep. 2019, doi: 10.1016/j.fusengdes.2019.02.090.

[19] K. Soni et al., "Effect of 3 T magnetic field on RF plasma sputtering in an ITER-relevant first mirror unit," *Nucl. Fusion*, vol. 62, no. 12, Dec. 2022, Art. no. 126009, doi: 10.1088/1741-4326/ac8b20.

[20] K. Soni et al., "Study of wall re-deposition on DC-grounded ITER-relevant mirrors with RF plasma in a first mirror unit," *Nucl. Fusion*, vol. 61, no. 12, Dec. 2021, Art. no. 126017, doi: 10.1088/1741-4326/ac2b74.

[21] K. Soni et al., "Deuterium plasma sputtering of mixed Be-W layers," *J. Nucl. Mater.*, vol. 564, Jun. 2022, Art. no. 153671, doi: 10.1016/j.jnucmat.2022.153671.

[22] A. Ushakov et al., "ITER visible spectroscopy reference system first mirror plasma cleaning in radio-frequency gas discharge–circuit design and plasma effects," *Fusion Eng. Design*, vol. 154, May 2020, Art. no. 111546, doi: 10.1016/j.fusengdes.2020.111546.

[23] P. Shigin et al., "RF discharge mirror cleaning system development for ITER diagnostics," *Fusion Eng. Design*, vol. 164, Mar. 2021, Art. no. 112162, doi: 10.1016/j.fusengdes.2020.112162.

[24] A. Ushakov et al., "Radio-frequency plasma to clean ITER front-end diagnostic mirrors in geometry of edge Thomson scattering system," *Phys. Scripta*, vol. 98, no. 1, Jan. 2023, Art. no. 015604, doi: 10.1088/1402-4896/aca5c5.

[25] S. Rajendran, "ITER remote handling code of practice," ITER IDM, Saint-Paul-lez-Durance, France, Tech. Rep. ITER_D_2E7BC5, v1.2, 2009.

[26] D. Samsonov et al., "First mirror unit and large-scale collecting mirror conceptual designs for ITER optical diagnostics," presented at the 31st Symp. Fusion Technol. (SOFT), Sep. 2020, doi: 10.13140/RG.2.2.14011.03367.

[27] D. Beltran, *EDH Part 4: Electromagnetic Compatibility (EMC)*, ITER IDM, document ITER_D_4B523E, v3.0, 2012.

[28] Y. Krasikov et al., "Main design features of the Rh-based first mirror developed for the ITER CXRS core diagnostics," *Fusion Eng. Design*, vol. 169, Aug. 2021, Art. no. 112408, doi: 10.1016/j.fusengdes.2021.112408.

[29] P. Mertens, "The core-plasma CXRS diagnostic for ITER: An introduction to the current design," *J. Fusion Energy*, vol. 38, nos. 3–4, pp. 264–282, Aug. 2019, doi: 10.1007/s10894-018-0202-1.

[30] U. Stephan et al., "Design and analysis of first mirror plasma cleaning electrical circuit for edge Thomson scattering ITER diagnostics," *Fusion Eng. Design*, vol. 177, Apr. 2022, Art. no. 113079, doi: 10.1016/j.fusengdes.2022.113079.

[31] S. Vives et al., "In-vessel final design of the ITER wide angle viewing system in equatorial port 12," *Fusion Eng. Design*, vol. 191, Jun. 2023, Art. no. 113734, doi: 10.1016/j.fusengdes.2023.113734.

[32] S. Vives et al., "Overview of optical designs of the port-plug components for the ITER equatorial wide angle viewing system (WAVS)," *Fusion Eng. Design*, vol. 146, pp. 2442–2445, Sep. 2019, doi: 10.1016/j.fusengdes.2019.04.014.

[33] A. Dmitriev, "D03—Analysis of power handling characteristics of MI cables and hollow feeders," ITER IDM, Saint-Paul-lez-Durance, France, Tech. Rep. ITER_D_VYKMFC v1.0, 2019.

[34] P. H. Smith, *Electronic Applications of the Smith Chart: In Waveguide, Circuit, and Component Analysis* (Classic Series), 2nd ed. Raleigh, NC, USA: Scitech Pub, 2006, ch. 9–10.

[35] S. Ramo, *Fields and Waves in Communication Electronics*, 3rd ed. Hoboken, NJ, USA: Wiley, 1994, sec. 4–10, pp. 198–200.

[36] D. W. Knight. (2016). *The Self-Resonance and Self-Capacitance of Solenoid Coils. Applicable Theory, Models and Calculation Methods*. [Online]. Available: http://dx.doi.org/10.13140/RG.2.1.1472.0887 and http://g3ynh.info

[37] V. Kustarev. (2016). *The Self-resonance Frequency*. [Online]. Available: https://coil32.net/theory/self-resonance-frequency.html

[38] V. P. Meschanov, I. A. Rasukova, and V. D. Tupikin, "Stepped transformers on TEM-transmission lines," *IEEE Trans. Microw. Theory Techn.*, vol. 44, no. 6, pp. 793–798, Jun. 1996, doi: 10.1109/22.506436.

[39] T. H. Lee, *Planar Microwave Engineering: A Practical Guide to Theory, Measurement, and Circuits*, vol. 1. Cambridge, MA, USA: Cambridge Univ. Press, 2004.

[40] L. G. Maloratsky, *Integrated Microwave Front-Ends With Avionics Applications*. Norwood, MA, USA: Artech House, 2012.

[41] S. J. Orfanidis. (2016). *Electromagnetic Waves and Antennas*. [Online]. Available: https://www.ece.rutgers.edu/~orfanidi/ewa/

[42] J. R. Whinnery and H. W. Jamieson, "Equivalent circuits for discontinuities in transmission lines," *Proc. IRE*, vol. 32, no. 2, pp. 98–114, Feb. 1944, doi: 10.1109/jrproc.1944.229737.

[43] M. G. Harrison, "Equivalent lumped parameters for a bend in a two-wire transmission line," Defense Tech. Inf. Center, Fort Belvoir, VA, USA, Tech. Rep. AFWL-TR-77-5, Jul. 1977, doi: 10.21236/ADA042038.

[44] J. R. Reid, E. D. Marsh, and R. T. Webster, "Micromachined rectangular-coaxial transmission lines," *IEEE Trans. Microw. Theory Techn.*, vol. 54, no. 8, pp. 3433–3442, Aug. 2006, doi: 10.1109/TMTT.2006.879133.

[45] M. N. O. Sadiku and C. N. Obiozor, "Finite element computation of the characteristic impedance of transmission lines," in *Proc. IEEE SOUTHEASTCON Eng. New Century*. Blacksburg, VA, USA: IEEE, 1997, pp. 166–168, doi: 10.1109/SECON.1997.598644.

[46] G. W. Slade and K. J. Webb, "Computation of characteristic impedance for multiple microstrip transmission lines using a vector finite element method," *IEEE Trans. Microw. Theory Techn.*, vol. 40, no. 1, pp. 34–40, Jan. 1992, doi: 10.1109/22.108320.

[47] G. Lentini, *CAD Manual 12-2 Piping Design*, document ITER_D_33WL3N, v1.2, ITER IDM, 2010.

[48] S. Chiocchio and K. Grosset, *Project Requirements (PR)*, document ITER_D_27ZRW8, ITER IDM, v6.3.

[49] C. Hazelton, J. Rice, L. L. Snead, and S. J. Zinkle, "Effect of neutron radiation on the dielectric, mechanical and thermal properties of ceramics for RF transmission windows," *J. Nucl. Mater.*, vol. 253, nos. 1–3, pp. 190–195, Mar. 1998, doi: 10.1016/s0022-3115(97)00333-4.

[50] S. Kume, M. Yasuoka, S.-K. Lee, A. Kan, H. Ogawa, and K. Watari, "Dielectric and thermal properties of AlN ceramics," *J. Eur. Ceram. Soc.*, vol. 27, nos. 8–9, pp. 2967–2971, Jan. 2007, doi: 10.1016/j.jeurceramsoc.2006.11.023.

[51] R. W. Rice, "The compressive strength of ceramics," in *Ceramics in Severe Environments*, W. W. Kriegel and H. Palmour, Eds. Boston, MA, USA: Springer, 1971, pp. 195–229, doi: 10.1007/978-1-4684-3141-4_14.

[52] S. Takakuwa et al., "A new transient liquid phase bonding method using magnesium foil to bond copper plates to aluminum nitride substrates," *J. Mater. Sci., Mater. Electron.*, vol. 33, no. 13, pp. 10486–10493, May 2022, doi: 10.1007/s10854-022-08035-w.

[53] N. Iwase, K. Anzai, K. Shinozaki, O. Hirao, T. Thanh, and Y. Sugiura, "Thick film and direct bond copper forming technologies for aluminum nitride substrate," *IEEE Trans. Compon., Hybrids, Manuf. Technol.*, vol. CHMT-8, no. 2, pp. 253–258, Jun. 1985, doi: 10.1109/TCHMT.1985.1136501.

[54] J. Lv, Y. Huang, R. Fu, Y. Ji, B. Wu, and X. Liu, "AlN/Cu composite ceramic substrate fabricated using a novel TiN/AgCuTi composite brazing alloy," *J. Eur. Ceram. Soc.*, vol. 40, no. 15, pp. 5332–5338, Dec. 2020, doi: 10.1016/j.jeurceramsoc.2020.07.060.

[55] J. Hlina, J. Reboun, and A. Hamacek, "Study of copper thick film metallization on aluminum nitride," *Scripta Mater.*, vol. 176, pp. 23–27, Feb. 2020, doi: 10.1016/j.scriptamat.2019.09.029.

[56] H. Miyazakia et al., "Effect of high temperature cycling on both crack formation in ceramics and delamination of copper layers in silicon nitride active metal brazing substrates," *Ceram. Int.*, vol. 43, no. 6, pp. 5080–5088, Apr. 2017, doi: 10.1016/j.ceramint.2017.01.020.

[57] Z. Di, P. Li-Xia, Q. Ze-Ming, J. Biao-Bing, and Y. Xi, "Novel ultra-low temperature co-fired microwave dielectric ceramic at 400 degrees and its chemical compatibility with base metal," *Sci. Rep.*, vol. 4, no. 1, p. 5980, Aug. 2014, doi: 10.1038/srep05980.

[58] M. T. Sebastian, H. Wang, and H. Jantunen, "Low temperature co-fired ceramics with ultra-low sintering temperature: A review," *Current Opinion Solid State Mater. Sci.*, vol. 20, no. 3, pp. 151–170, Jun. 2016, doi: 10.1016/j.cossms.2016.02.004.

[59] E. E. Alyasova and D. L. Shimanovich, "Method of producing dielectric layer on aluminium substrate surface," RU Patent 2 694 430, 2018. [Online]. Available: https://patents.google.com/patent/RU2694430C1/en

[60] R. Juarez, *D11-3—Determination of Quantities in EP N11 During Machine Operation As Per Section 6.3.2*, document ITER_D_Y86WVS, ITER IDM, v1.0, 2020.

[61] M. J. Loughlin and N. P. Taylor, *Recommendation on Plasma Scenarios*, document ITER_D_2V3V8G, ITER IDM, v1.2, 2009.

[62] T. Yano and T. Iseki, "Swelling and microstructure of A1N irradiated in a fast reactor," *J. Nucl. Mater.*, vol. 203, no. 3, pp. 249–254, Sep. 1993, doi: 10.1016/0022-3115(93)90381-8.

[63] T. Yano and T. Iseki, "Thermal and mechanical properties of neutron-irradiated aluminum nitride," *J. Nucl. Mater.*, vols. 179–181, pp. 387–390, Mar. 1991, doi: 10.1016/0022-3115(91)90106-h.

[64] T. Pornphatdetaudom, T. Yano, and K. Yoshida, "Physical property changes of neutron-irradiated aluminum nitride and their recovery behavior by annealing using a step-heating dilatometer," *Nucl. Mater. Energy*, vol. 16, pp. 24–28, Aug. 2018, doi: 10.1016/j.nme.2018.05.027.

[65] T. Yano, Y. Futamura, M. Imai, and K. Yoshida, "Recovery behavior of neutron-induced damage of AlN irradiated at higher temperatures by thermal annealing," *J. Nucl. Mater.*, vol. 440, nos. 1–3, pp. 495–499, Sep. 2013, doi: 10.1016/j.jnucmat.2013.02.025.

[66] T. Yano, M. Tezuka, H. Miyazaki, and T. Iseki, "Macroscopic length, lattice parameter and microstructural changes in neutron-irradiated aluminum nitride due to annealing," *J. Nucl. Mater.*, vols. 191–194, pp. 635–639, Sep. 1992, doi: 10.1016/s0022-3115(09)80124-4.

[67] R. Feder, M. Youssef and J. Klabacha. (2013). *The Status of USITER Diagnostic Port Plug Neutronics Analysis Using Attila*. [Online]. Available: https://www.osti.gov/servlets/purl/1148887

[68] Y. Zhai et al., "Design and analysis progress of U.S. ITER diagnostic upper port #14," *IEEE Trans. Plasma Sci.*, vol. 46, no. 5, pp. 1641–1647, May 2018, doi: 10.1109/TPS.2018.2791348.

[69] R. S. Afanasenko et al., "Nuclear heat loads to the first mirror unit of H-alpha diagnostic in the ITER equatorial #12 port," *Problems At. Sci. Technol., Ser. Thermonuclear Fusion*, vol. 43, no. 3, pp. 24–30, 2020, doi: 10.21517/0202-3822-2020-43-3-24-30.

[70] I. Orlovskiy, E. Andreenko, and A. Alekseev, "Estimation of neutral fluxes on the first mirror of H-alpha diagnostics in ITER," *Fusion Eng. Design*, vol. 146, pp. 827–830, Sep. 2019, doi: 10.1016/j.fusengdes.2019.01.091.

[71] D. Samsonov, *D5—Preliminary Results of Structural Calculations of FMU and Corresponding Vibrational Spectra*, document ITER_D_3F4D2G, ITER IDM, v1.1, 2020.

[72] A. Birbraer, *Seismic Analysis of Structures*. St.-Petersburg, Russia: Nauka, 1998.

[73] V. Barabash, *AC01-2102 Steel 660—Yield Strength*, document ITER_D_223JMT, ITER IDM, v1.0, Art. no. 2007.

[74] T. L. Anderson, *Fracture Mechanics: Fundamentals and Applications*, 4th ed. Boca Raton, FL, USA: CRC Press, 2017, sec. 2.6.2 and 2.6.3, pp. 47–55.

[75] M. F. Ashby and D. R. H. Jones, *Engineering Materials 2: An Introduction to Microstructures and Processing*, 4th ed. Amsterdam, The Netherlands: Elsevier, 2013.

[76] H. Abe, M. Naito, T. Hotta, N. Shinohara, and K. Uematsu, "Flaw size distribution in high-quality alumina," *J. Amer. Ceram. Soc.*, vol. 86, no. 6, pp. 1019–1021, Jun. 2003, doi: 10.1111/j.1151-2916.2003.tb03411.x.

[77] T. Fett and D. Munz, "Failure behavior of ceramics for gyrotron windows," *Fusion Technol.*, vol. 32, no. 2, pp. 170–178, Sep. 1997, doi: 10.13182/fst97-a19889.

[78] A. G. Evans and S. M. Wiederhorn, "Proof testing of ceramic materials? An analytical basis for failure prediction," *Int. J. Fract.*, vol. 10, no. 3, pp. 379–392, Sep. 1974, doi: 10.1007/bf00035499.

[79] W. Eckstein et al., "Sputtering data," IPP, Garching, Germany, Tech. Rep. IPP 9/82, 1993.

[80] E. W. Thomas et al., "An evaluated data base for sputtering," IAEA, Vienna, Austria, Tech. Rep. INDC(NDS)-287, 1993.

[81] A. M. Dmitriev et al., "Re-deposition of ITER-grade be on plasma gun facility QSPA-be: Characterization & plasma cleaning," *Nucl. Mater. Energy*, vol. 30, Mar. 2022, Art. no. 101111, doi: 10.1016/j.nme.2021.101111.

[82] B. Andries, G. Ravel, and L. Peccoud, "Electrical characterization of radio-frequency parallel-plate capacitively coupled discharges," *J. Vac. Sci. Technol. A, Vac., Surf., Films*, vol. 7, no. 4, pp. 2774–2783, Jul. 1989, doi: 10.1116/1.576177.